Journal of Quantitative Spectroscopy & Radiative Transfer 245 (2020) 106848

Contents lists available at ScienceDirect

Journal of Quantitative Spectroscopy & Radiative Transfer

journal homepage: www.elsevier.com/locate/jqsrt

CDSDv: A compact database for the modeling of high-temperature CO_2 radiation

João Vargas[a,1,*], Bruno Lopez[b,2], Mário Lino da Silva[c,3]

[a] Instituto de Plasmas e Fusão Nuclear, Instituto Superior Técnico, Universidade de Lisboa, Av. Rovisco Pais 1, Lisboa, 1049-001, Portugal
[b] Department of Aerospace Engineering, University of Illinois at Urbana-Champaign, 306 Talbot Lab, 104 S. Wright St., Urbana, 61801, IL, USA
[c] Instituto de Plasmas e Fusão Nuclear, Instituto Superior Técnico, Universidade de Lisboa, Av. Rovisco Pais 1, Lisboa, 1049-001, Portugal

ARTICLE INFO

Article history:
Received 20 December 2019
Revised 20 January 2020
Accepted 20 January 2020
Available online 28 January 2020

Keywords:
CO_2
IR Radiation
Database
High-Temperature

ABSTRACT

The Carbon Dioxide Spectral Databank 4000 is tailored for radiative transfer applications relevant for Mars atmospheric entry studies. This is carried out through the refitting of the original database, encompassing individual rovibrational transitions, into a more compact form where rotational transitions for specific vibrational bands are obtained through traditional polynomial expressions, fitted to the levels and transitions of the original database. This originates a certain loss of precision since the fitted expressions do not always reproduce the original data with full accuracy, namely for the perturbed transitions. This is offset by a more compact database suited for wideband radiative transfer simulations. This CDSDv database also provides some minor advantages, such as enabling the thermodynamic use of two-temperature (T, T_v) models and the determination of vibrational Einstein coefficients $A_{v'v''}$ which may be used in state-to-state kinetic models.

1. Introduction

Radiative heat transfer from CO_2 infrared transitions has been recognized [1,2] to be a driver for exploration spacecraft design (with an emphasis on the backshell). This has led several research teams to adapt existing databases [3,4] or develop new ones [5] for this purpose. The advent of the Carbon Dioxide Spectral Databank (CDSD), particularly it's high-temperature version CDSD4000 [6], provided the community with a powerful tool for estimating the high-temperature radiative properties of CO_2. Nevertheless, this database follows a spectrally-ordered structure, with the definition of cutoff thresholds for single lines based on a specific temperature (4000K in the case of CDSD4000). This makes it less than optimal for spacecraft radiative heating calculations [7], where the inclusion the overall spectral range of CO_2 transitions is mandatory. Further, the post-shock flow surrounding the spacecraft has a wide range of temperatures, from abour 5000–6000 K in the shock layer, down to 1000K or less in the afterbody wake. It has consequently been decided to adapt this CDSD database for such purposes: Firstly the database has been modified from a spectrally ordered to a transition-ordered database. Then, each band of rovibrational transitions has been fitted to a general polynomial expansion consistent with the theory of radiation from linear triatomic molecules[8]. Although this technique means a certain loss of accuracy, particularly for transition between higher-lying vibrational levels which exhibit a certain amount of perturbations, it has the benefit of yielding a more compact and tractable database (16 MB down from 16GB). Another added benefit stems from the explicit separation of the vibrational and rotational part of the transitions, which allows using two-temperature (Tv, Tr) models, or using the corresponding Einstein coefficients $A_{v'v''}$ in vibrationally-specific state-to-state models.

This work will firstly discuss in detail the legacy of past Mars exploration spacecraft designs, and the associated Computational Fluid Dynamics (CFD) and radiative models that have been deployed to support such designs. This is carried out in Section 2. Section 3 describes the theoretical models and reduction techniques that have been applied for creating this compact CDSD database (henceforth named CDSDv). Section 4 presents some sample comparisons of CDSDv with other popular CO_2 radiative databases, alongside some numerical benchmarks, highlighting the speedup and memory optimization brought by CDSDv. Finally

---

* Corresponding author.

E-mail addresses: joao.f.vargas@tecnico.ulisboa.pt (J. Vargas), belopez@illinois.edu (B. Lopez), mlinodasilva@tecnico.ulisboa.pt (M.L.d. Silva).

[1] PhD candidate, Instituto de Plasmas e Fusão Nuclear, Instituto Superior Técnico, Universidade de Lisboa. Former visiting scholar at Department of Aerospace Engineering, University of Illinois at Urbana-Champaign.

[2] Associate Researcher, Department of Aerospace Engineering, University of Illinois at Urbana-Champaign.

[3] Assistant Professor, Department of Physics, Instituto de Plasmas e Fusão Nuclear, Instituto Superior Técnico, Universidade de Lisboa.

https://doi.org/10.1016/j.jqsrt.2020.106848
0022-4073/

Section 5 validates the CDSDv database against popular testcases from the literature. The conclusions summarize the capabilities of CDSDv, highlighting its flexibility and providing a qualitative assessment of the tradebacks in accuracy compared to CDSD4000. Finally suggestions for future improvements of this database are shortly presented.

2. Aerothermal and radiative databases for Mars exploration missions

It is somehow surprising that the issue of CO_2 radiation influence on Martian entries has been discarded up until so recently. It may further seem surprising that this did not preclude many spacecraft from successfully reaching Mars, however this can in part be attributed to the engineering margins considered in these spacecraft designs, and the fact that radiative heating typically remains inferior to convective heating, except in the base region where it doesn't lead to excessively high heat fluxes owing to the low densities encountered in this recirculation region.

The first efforts to correctly account for CO_2 IR heating may be traced to the Mars PREMIER program [9,10] sponsored by the French Space Agency CNES[4] and the AURORA program [11] sponsored by the European Space Agency (ESA) which took over once the Mars PREMIER program was terminated. These took place in the beginning of the 21st Century, and gathered several European and Russian research teams, which undertook some early works outlining the importance of these effects. Later on, the importance of these radiative heating effects was also acknowledged by several research teams in the US which provided additional key contributions, namely at the experimental level. Here, we will briefly outline the different US and Russian missions that were launched towards Mars without accounting for any radiative heating effects (all the Russian Mars exploration missions, and all the US Mars exploration missions up to Mars Science Laboratory in 2012), we follow by an historical account of the different efforts that led to this phenomena being nowadays recognized as an important design driver for Mars missions.

2.1. USSR/Russia mars missions

All USSR/Russian missions to Mars have failed to achieve a successful landing. Mars 2 crashed, Mars 3 successfully landed but stopped transmitting after 20s, Mars 6 lost contact prior to landing, Mars 7 missed Mars, and Mars 8 (Mars 96) suffered a failure during the injection to a trajectory towards Mars and reentered the atmosphere.

2.2. US Mars missions (pre-2012)

US Mars exploration missions have historically neglected CO_2 IR radiative heating until very recently.

The second lander to touch down the surface of Mars, Viking 1 in 1976, was developed without any previous test carried out in a ground test facility simulating a Martian-like CO_2 atmosphere [12]. It nevertheless was the first lander to successfully touch down the surface of Mars[5], following an atmospheric entry at a velocity of 4.5km s^{-1} and an entry angle of 11° [13,14]. The Viking probe was instrumented with stagnation pressure and temperature sensors, as well as four additional pressure transducers and a mass spectrometer in the forebody. The backshell had an additional pressure transducer and two thermocouples. This entry data has since been extensively reviewed and rebuilt by several authors, since it constituted for many years the only available post-flight data for a Martian entry [12].

Pre-flight analysis predicted that afterbody heating would account for 3% of stagnation-line heating, and that radiation would be totally negligible owing to the low entry velocity [12]. However 5% heating relative to stagnation-line heating reference was measured instead. Recent reinvestigations accounting for CO_2 radiative heating showed that this difference might indeed be due to neglecting these heating effects in the original analysis [15,16].

The subsequent 1996 Mars pathfinder mission considered a faster entry at a velocity of around 7.5 km s^{-1}. Pre-flight studies had to consider ablation effects in the CFD analysis, however radiation heating effects were once more neglected [12], with Gupta's prediction that radiative heating would account for less than 4.5% of total heating [17]. The probe was instrumented with accelerometers, 9 thermocouples, and 3 platinum resistance thermometers. These last did not perform well due to calibration problems, with only the thermocouple data being valid [12]. Pre-flight experimental campaigns were carried in the HYPULSE shock-expansion tube with different gas mixtures including CO_2, with negligible dissociation in the freestream flow [18], and the NASA LaRC 31 Mach 10 wind-tunnel for estimating the probe wake flow. These last experiments were carried solely on air [19].

Other NASA missions like the Mars Polar Lander (6.9 km s^{-1}; failure during entry), Mars Exploration Rovers (5.4 km s^{-1}; success; for MER-A and 5.55 km s^{-1}; success; for MER-B), and Phoenix (5.7 km s^{-1}; success) missions, made use of the same assumptions regarding radiation (see Reynier [12] and references therein). These probes were not instrumented as regarding their entry phases, and as such, no post-flight data is available for these.

The following mission, Mars Science Laboratory, is the largest space vehicle to ever have entered Mars, having done it successfully. The probe has a 4.5 m diameter, and entered Mars at 5.6 km s^{-1} in 2012. Owing to the increased risks for this mission, it underwent an extensive pre-flight test campaign, namely in which pertains to transition to turbulence effects. Several tests were carried out in the CUBRC LENS and Caltech T5 shock tunnels [12]. The probe itself had an extensive instrumentation package named MEDLI, which monitored temperature, pressure and TPS (Thermal Protection System) performance in the probe forebody. No radiative heating sensors were included, as radiation was again considered negligible [12,20]. Ref. [21] provides a synthesis of all the experimental and numerical activities carried out in preparation of this mission.

2.3. Acknowledging the impact of CO_2 radiation

As mentioned before, European efforts regarding Mars exploration may be traced back to the Mars PREMIER/Mars Sample Return project, a joint CNES/NASA venture aiming at a return of Samples from Mars surface to Earth. The early mission definition consider direct aerocapture insertion of the Mars Sample Return Orbiter (MSRO) designed by CNES [22–24]. The challenges for performing such a manoeuver[6] (requiring precise guidance as the orbiter descends significantly in Mars atmosphere), and the high thermal loads involved (mandating an heat shield), fostered several European research activities related to Mars entry aerothermodynamics. For example two Ph.D. thesis were funded by this program, one related to the modelling of free-molecular CO_2–N_2 flows [25], and the other related to CO_2-N_2 plasmas radiation [26].

Ultimately, difficulties in enabling such an ambitious programme, funding difficulties, as well as a shifting political cli-

---

[4] in collaboration with NASA, as a staging for a Mars Sample Return mission

[5] following the failure of the USSR Mars 3 mission

[6] which only has been partially achieved by the Russian Zond 6 and Zond 7 probes during their Lunar return trajectories

mate, led to the cancellation of this programme. In the meanwhile, ESA had launched the AURORA programme, chiefly aimed at the robotic exploration of Mars, as a stepping stone to a Mars Sample Return mission and ultimately a manned Mars exploration mission. A workshop titled “Radiation of High-Temperature Gases in Atmospheric Entry” (RHTGAE) has been held biannually since 2003, which has been chiefly focused on the radiative heating effects of atmospheric entry flows [27–35]. The workshop defined a set of testcases tailored for the examination of radiative properties for gases of different compositions and different levels of thermodynamic equilibrium (ranging from thermochemical equilibrium to strong nonequilibrium of the species internal modes). Among these, the TC3 testcase focused on a 70° sphere-cone geometry which is a simplified configuration of the MSRO vehicle [36,37]. Reference CFD solutions were proposed to the teams who wished to only simulate radiative transfer, but nevertheless, a significant number of CFD simulations were also carried out by different teams. An INTAS project [38] was further devoted to the TC3 configuration, including CFD, radiative transfer and ground-test experiments of a scale model [39]. This work was carried out by five Russian (ICAD, IPM, NIIMech, SPU, TsAGI), and two European institutions (Office national d’études et de recherches aérospatiales, ONERA and Von Karman Institute, VKI).

Radiative heating for this spacecraft configuration has been modelled considering different numerical approaches and using different radiative databases: The EM2C team at École Centrale de Paris used their in-house HITELOR radiative database [40,41], based on a statistical narrow-band model, and developed from a set of CO_2 and CO spectral coefficients valid at high temperature, obtained both in-house and adapted from the HITEMP database [42]. The databank has been successfully applied to the reproduction of medium-resolution spectra at temperatures up to 2850K [43]. Radiative transfer on the backcover of TC3 was carried out using a Ray-Tracing model, considering both line-by-line and statistical narrowband models. The agreement of the obtained results for both the reference (line-by-line) and the approximate (statistical narrowband) models validated the later approach, for the one-temperature case, allowing fast and efficient simulations of CO_2 IR radiation in this configuration. These results were presented at the 1st. RHTGAE workshop [44].

Surzhikov used increasingly refined CFD and radiative approaches since 2001 [45], where a one-temperature, chemical nonequilibrium CFD model was used coupled to a multigroup radiative database based on HITRAN. Radiative transfer was modeled using a modified discrete ordinates method. Further works considered improved physical models, namely in what pertains to CFD simulations, where multitemperature models, including the influence of thermal nonequilibrium on chemistry, were considered [46,47]. A coupling between flow and radiation was ensured by injecting the divergence of radiative flux in the energy equation for the CFD model. This model was applied to the TC3 testcase, with the determination of a CFD solution and the subsequent calculation of radiative heating [48]. The computed heat fluxes were in agreement with the previous solutions from EM2C. Surzhikov also carried CFRD (Computational Fluid Radiative Dynamics) simulations on other US Mars entry vehicles, namely Pathfinder [49,50] and Mars Science Laboratory [50]. As for TC3, it was found that radiative heating from the IR region was not negligible, even exceeding convective heating in some regions of the leeward flow.

In 2002, ONERA started developing the PHARAON computing chain, comprised of the CelHyo2D CFD solver [51,52], coupled to the radiative heat transfer solver ASTRE, which is a Monte Carlo solver enabling the treatment of 3-D geometries using unstructured meshes [53–55]. The ASTRE code was initially developped for the study of turbulent flames in the presence of soot. The EM2C radiative database is utilized by this platform. The simulation results for the TC3 test-case were presented in Ref. [56], with again the same results than the previous authors.

Finally, IPFN-IST (Instituto de Plasmas e Fusão Nuclear - Instituto Superior Técnico) relied on the CO_2-N_2 radiative database developed by Lino da Silva [26], implemented in the SPARTAN Line-by-Line code [5,57]. The CO_2 database was developed from the 1992 HITRAN database [58], using the same theoretical approach than the one used for developing the HITELOR database [42]. Radiative transfer for the TC3 configuration was computed using a ray-tracing approach, both for the forebody and the backshell, considering the reference two-temperature solution from the workshop booklet [59]. This work found essentially the same results than the previous ones, and further found that the influence of thermal nonequilibrium did not have a significant impact on the computed radiative heat fluxes. Further applications of this radiative database were carried out in the scope of the unsuccessful tracking of the PHOENIX entry by the Mars Express orbiter, as it was not capable of switching its IR thermal detectors. CFD simulations were carried with a DSMC (Direct Simulation Monte Carlo) code, and a simplified radiative transfer model showed that the IR radiative signal would be several orders of magnitude above the VUV signal (from the CO 4th Positive system). The outcome of this work was published in Ref. [60,61].

These different results obtained for TC3 showed good agreement regarding the radiative heating trends and absolute values. Radiative heating in the forebody remained within the margins of convective heating, however in the backcover it exceeded significantly the convective heating values, due to the radiation from the spacecraft wake. Namely, the radiative heating values (in the order of $W\ cm^{-2}$) were deemed too large, requiring for the backshell to have a certain amount of thermal protections.

2.4. Mars exploration missions planning (post-2012)

The ESA EXOMARS mission was the first Mars Exploration mission that was designed considering the effects of CO_2 and CO IR radiative heating. Initial plans accounted for a single mission of a large entry vehicle carrying a rover. However, this required a heavy launcher (PROTON-M/Ariane-5). Further, it was found that the radiative fluxes would mandate a backshell TPS of about 12kg. Eventually, these uncertainties, as well as the necessity of testing Mars entry technologies for what was an European first, led to a redefinition of the program into a two-stage mission: A first launch of an orbiter (Mars Trace Gas Orbiter) and a fully instrumented lander in 2016, followed by a second launch of a larger lander including the rover in 2018 (since then postponed to 2020). The Phase B of the mission was managed by Fluid Gravity Eng., who performed the CFD simulations. IPFN-IST performed radiative transfer calculations using the same ray-tracing model than for TC3. A further code-to-code comparison was carried out by Surzhikov, who simulated the same spacecraft configurations [62]. As for the TC3 test case, the simulation results showed that over 99.95% of radiative heating would come from CO_2 and CO IR radiation [63]. Another interesting feature of the probe was its instrumentation package, who was capable of determining static pressure, surface temperatures, radiative heat flux rates and total heat flux rates, both in the forebody and backshell.

Schiaparelli entered Mars atmosphere on the 19th October 2016, at a velocity of about 5.8 $km\ s^{-1}$, and collected data from its sensor package throughout all of its entry phase. This data was relayed to the orbiter and retrieved in its entirety, except for the blackout phase data that was stored for a later post-landing transmission. Unfortunately the probe was lost due to a software malfunction which led to the premature stopping of the descent engines and the discarding of the descent parachute. As such, the data for the blackout phase, including the peak radiative heating, was lost. Nevertheless the retrieved data still contains an interesting amount of information which makes it useful for a test-case. The details on the post-processing for this data may be found in Ref. [64].

Further developments in the US, roughly after the Mars Science Laboratory mission, started looking into the issue of IR radiation with more detail. For example, teams from NASA Ames participated in the later issues of the ESA radiation workshop, and this fostered an interest in trying to measure experimentally IR radiation from CO_2 flows in shock-tubes and shock-tunnels, which provided the more realistic ground-test conditions. Around that time, the EAST shock-tube was in the process of being refurbished, alongside with its instrumentation, therefore efforts were put into achieving a capability for carrying measurements in this spectral region [65]. A first batch of CO_2 IR measurements was carried out in EAST around 2010 [66], which confirmed the presence of a strong radiative signal. Around the same time the numerical tools for radiative prediction were being overhauled. Although some works had been carried out in the 90's regarding IR radiation in wake flows [67], there had been no follow-up since, and radiative tools like NEQAIR were lacking the appropriate spectral models. As the CDSD4000 database was published around this time [6], it was integrated to the NEQAIR line-by-line code, using a simplified pseudo-continuum approach [68]. Since then, more detailed experimental campaigns were carried out on EAST, focusing on Mars entries [69]. These works further cemented the relevance of CO_2 IR heating in the scope of NASA missions for Mars exploration [70]. Lastly, the Mars Science Laboratory flight data was reinterpreted in view of the presence from CO_2 radiation [71], and the available Schiaparelli flight data was also reproduced recently to a good agreement with these new improved radiative models [72].

Nowadays, no question remains about the necessity to account for IR radiative heating in Mars entry flows, and all aerothermal databases account for these effects in one way or another, which allows reducing the uncertainties in TPS design, leading to lighter TPS, more room for payloads, and more confidence in designing ever larger entry spacecrafts in preparation of a Manned Mars mission.

3. Methods

Here we summarize the underlying theory for linear triatomic molecules radiation, which was put to use in reducing the CDSD4000 database into CDSDv. Expressions for level energies, transition probabilities, and broadening are discussed in this section, which concludes with a discussion of the database re-fitting algorithm

3.1. CDSD Structure

Ro-vibrational databases such as HITRAN [3] and CDSD [6,73] adopt a similar format. Each data entry in CDSD contains all the parameters in Table 1 spectrally organized. Not all the parameters are necessary for the processing done in this work. The first half of the table contains the parameters that are needed for this work while the parameters on the second half may be discarded. Table 1 does not present the data ordered as it is in CDSD. In the case of CDSD4000 there are 2769 different files which represent over 72 GB when in a uncompressed format. Besides featuring the four main isotopes of `CO2` by terrestrial abundance, CDSD also features transitions in which the upper, lower or both levels could not be spectroscopically assigned reliably. Partially or totally unassigned transitions are excluded from the treatment presented in the scope of this work. Also excluded are isotopes other than 626.

3.2. Lineshape algorithm

One of the advantages of not setting a line strength cut-off in the database generation step is the ability of applying the cut-off on the fly. In this work this is largely done by a routine that has already been described in [57]. This routine, henceforth 'lineshape routine', still warrants a brief discussion for the purposes of this work. It receives as input the line position, emission and absorption coefficients, and the Lorentzian and Gaussian broadening parameters. The user is allowed to set numerical coefficients that separate the input lines into strong lines or weak lines, therefore automatically applying a cut-off to the input database. Strong lines are treated in greater detail, wherein an algorithm detects possible overlap of nearby lines and new lineshapes are only calculated if they are significantly different in shape than the previous one, thereby saving further computational time. Weak lines are treated as a pseudo-continuum by bundling the individual line contributions over a coarse discretization of the full spectrum. This further decreases the computational effort necessary to compute a detailed spectrum. By itself, this method should provide a significant increase in the overall performance of spectrum calculations with CDSD4000. By further decreasing the total number of transitions by using CDSDv, an additional increase in performance should be expected. Some attention is devoted in trying to separate these contributions in Section 4.3.

3.3. Lorentz FWHM determination

From Table 1, the data used for computing the Lorentz FWHM (or HWHM) of a line and it's shift is ignored. Databases such as CDSD and HITRAN choose to compute pressure broadening by a semi-empirical expression that accounts, with fitted coefficients, for the broadening of ro-vibrational lines caused by self-broadening and air-broadening for any pressure and temperature conditions from a reference value at standard pressure and temperature. This approach, while straightforward, neglects the effect of other species in the calculation of the FWHM of Lorentz broadening. In this work we have opted for a more complex approach that accounts for the different broadening effects by generalized and specific expressions for each effect. While these general expressions are often approximations and not valid universally, they do offer a more flexible approach to different conditions and gas mixtures that ro-vibrational state of the art databases do not possess. These statements are not meant as a final judgement on the approaches that should be used but more of a comment on the relative merits and disadvantages of both methods. While both approaches will be close in value at low temperature, enough for a relatively fair comparison of lineshape calculation, the values will diverge for other conditions which will not yield a fair comparison between lineshape calculations using different methods. This is mitigated by the fact that Lorentz broadening is only expected to be significant at high pressures and low temperatures while Doppler broadening, which can be computed through an analytical expression, will be dominant at higher temperatures. The theoretical expressions for the different broadening mechanisms are summarized below. Resonance broadening adapted from [5]:

$$\Delta\overline{\nu} = K_1 \sqrt{\frac{g_u}{g_l}} A_{ul} \frac{N_l}{\overline{\nu}^3} \tag{1}$$

where $K_1 = 1.2893 \times 10^{-19}$, g_u and g_l the upper and lower degeneracies, A_{ul} the Einstein coefficient, N_l the lower level number density in m^{-3} and $\overline{\nu}$ the line position in cm^{-1}. Van der Waals broadening adapted from [74]:

$$\Delta\overline{\nu} = K_2 \frac{2}{c_0} \sqrt{\frac{2T_{gas}}{M_{avg}}} N_{tot} \overline{\nu}^2 \tag{2}$$

Table 1
Description of parameters format for CDSD-4000. The parameters in the first half of the table are the ones used in the refitting. Some parameters of the lower half of the table are saved for possible future reference but are not used in the refitting. The data is not ordered as represented in this table. [6].

Symbol	Parameter	Comment
I	Isotope index	Ordered by terrestrial abundance
$\overline{\nu}$	Line position	cm^{-1}
A	Einstein A-coefficient	s^{-1}
E''	Lower state energy	cm^{-1}
v_1', v_2', l_2', v_3', r'	Upper state vibrational numbers	
v_1'', v_2'', l_2'', v_3'', r''	Lower state vibrational numbers	
b	Branch	P, Q or R
J''	Lower state J	
w"	Lower state Wang symmetry	e or f
M	Molecule	$M = 2$ for CO_2
S	Intensity	cm^{-1}/(part.cm^{-2}) at 296K
γ_{air}	Air-broadened half-width	cm^{-1}atm^{-1} at 296 K
γ_{self}	Self-broadened half-width	cm^{-1}atm^{-1} at 296 K
n_{air}	Temperature-dependence exponent for γ_{air}	
δ_{air}	Air pressure-induced line shift	cm^{-1}atm^{-1} at 296 K
n_{self}	Temperature-dependence exponent for γ_{self}	
p', c', n'	Upper state polyad, Wang symmetry and ranking number	$c = 1$(e) or $c = 2$(f), $n' = r'$
p'', c'', n''	Lower state polyad, Wang symmetry and ranking number	$c = 1$(e) or $c = 2$(f), $n'' = r''$

where $K_2 = 1.95 \times 10^{-28}$, c_0 the speed of light in m/s, T_{gas} the gas temperature, M_{avg} the average molar mass of the mixture in kg/mol, N_{tot} the total number density in m^{-3} and $\overline{\nu}$ the line position in cm^{-1}. Collisional broadening adapted from [5]:

$$\Delta\overline{\nu} = \frac{2}{c_0}\sqrt{8k_B\pi T_{gas}}\sum_i \frac{N_i}{\sqrt{\mu_{red}}}(r_i + R)^2 \tag{3}$$

where c_0 the speed of light in m/s, k_B the Boltzmann constant, T_{gas} the gas temperature, N_i the number density of perturbing species i in m^{-3}, μ_{red} the reduced mass of the radiative and perturbing species system, r_i the radius of perturbing species i in meters and R the radius of the radiative species.

3.4. Selection rules and rotational branches

CO_2 is a linear triatomic molecule with 3 degrees of vibrational freedom, symmetric stretching denoted v_1, bending denoted v_2 and asymmetric stretching v_3. The bending mode is also associated with the vibrational angular momentum l_2 with possible values v_2, $v_2 - 2$, ..., 1 or 0. If $l_2 = 0$ only even or odd rotational numbers exist besides $J = 0$. Furthermore, rotational levels have alternating e/f parity such that if level J has e parity $J + 1$, if it exists, has f parity. Rotational levels also have an absolute minimum equal to l_2 which does not mean that the lowest rotational number of a level is the same as l_2 but rotational levels which are below l_2 do not exist. The collection of numbers $\{v_1, v_2, l_2, v_3, J\}$ plus the parity label constitute the spectroscopic assignment of a ro-vibrational level of CO_2. The selection rules for ro-vibrational electric dipole transitions on a linear triatomic molecule allow for three different cases [8]:

1. $\Delta l = l_2' - l_2'' = 0$ and $l = 0$, only has P and R branches.
2. $\Delta l = l_2' - l_2'' = \pm 1$, has P and R branches with a strong Q branch.
3. $\Delta l = l_2' - l_2'' = 0$ and $l \neq 0$, has P and R branches with a weak Q branch which is not always observed experimentally.

The branches, P, Q and R occur when $\Delta J = J' - J''$ is -1, 0 or 1 respectively. Additionally the selection rules for e/f parity apply: for P and R branches parity must be conserved (e ↔ e or f ↔ f) and for Q branch parity must be changed (e ↔ f). The possible ro-vibrational transitions between two vibrational levels are illustrated in Fig, 1 assuming that all rotational levels exist, i.e. that both v' and v'' have $l_2 > 0$. Care must be taken when dealing with cases 2 and 3 as the alternating parity of rotational numbers can create two different transition groups, one group with P, R branches ending in e levels and Q branches ending in f levels and another group with P, R branches ending in f levels with Q branches ending in e levels. Separate treatment of the same transition is necessary especially for higher rotational numbers as the separation between e and f levels becomes irregular and the two groups become distinct in their spectral position.

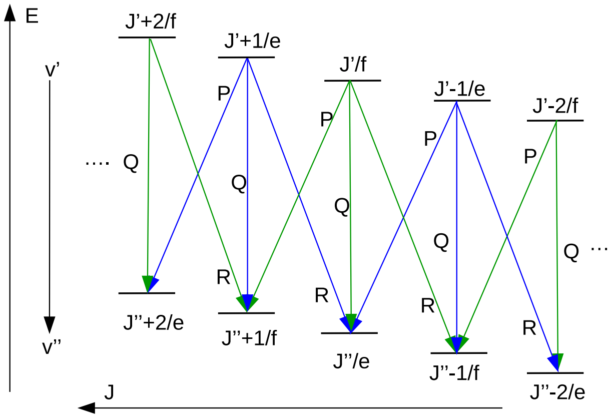

Fig. 1. Possible ro-vibrational transitions between upper and lower levels.

3.5. Energy level fitting

The energy E_{vJ} of a level with vibrational quantum state v and rotational state J have been fitted using the least squares procedure to the following expression:

$$E_{vJ} = G_v + B_v[J(J+1)] - D_v[J(J+1)]^2 + H_v[J(J+1)]^3 \tag{4}$$

Inevitably several fits will be performed on the same level v', most of which are discarded as only the fit with the smaller squared norm of the residual is kept. Some extrapolation may be required as the fit was performed between a J_{min} and J_{max}. If J_{min} is higher than l_2, the rotational numbers in between will be missing. For every level, J_{min} is replaced by max(l_2, 1) if J_{max} is odd or max(l_2, 2) if J_{max} is even. The differentiated treatment ensures that J_{min} is consistent with the rotational numbers parity. J_{max} also needs to be extrapolated as usually the highest rotational level is not enough to cover the regions where the transition is not negligible. As such all fitted polynomials are considered to be valid up to

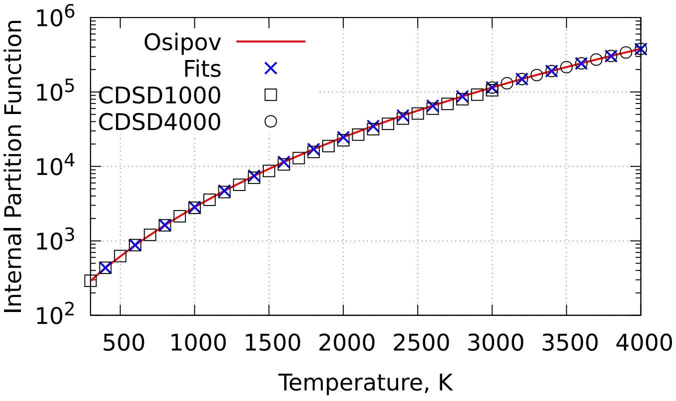

Fig. 2. Total internal partition function obtained through direct summation versus values from Osipov [75] and CDSD1000 [73] and CDSD4000 [6].

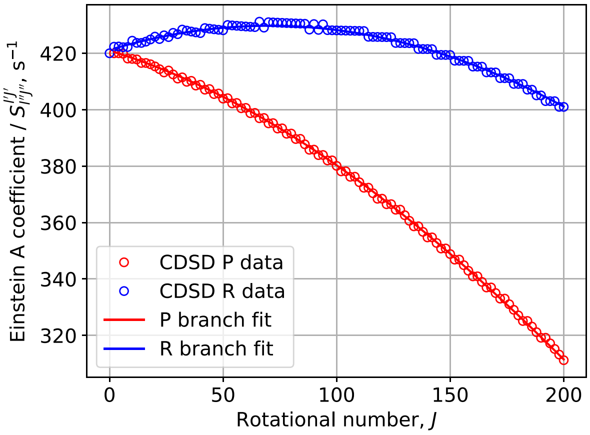

Fig. 3. Fitting example for transition 00011 → 00001.

$J_{\max} + 100$. This ensures that most of the relevant levels are covered and the partition function is recovered. As validation of this method, Fig. 2 presents the internal partition function calculated by direct summation compared with values from literature [75], CDSD1000 [73] and of CDSD4000 [6]. The partition function computed through this method is overlapped with the values from literature thus validating this approach.

3.6. Transition fitting

Vibrational transitions are related to ro-vibrational transitions through [5]:

$$A^{v'}_{v''} \times S^{l'J'}_{l''J''} \times F_{J'J''} = A^{v'J'}_{v''J''} \tag{5}$$

where $A^{v'}_{v''}$ are the vibrational Einstein-A coefficients, $S^{l'J'}_{l''J''}$ the Hönl-London factors, $F_{J'J''}$ the Herman-Wallis factors and $A^{v'J'}_{v''J''}$ the ro-vibrational Einstein-A coefficients. The Hönl-London factors account for the rotational separation of a vibrational transition into P, Q and R branches and are normalized by the factor $(2J' + 1)$. These factors are summarized in Table 2. The Herman-Wallis effect is a correction of the separation into rotational branches and is accounted for by the Herman-Wallis factor with a different form for each rotational branch [8]:

$$F^{P}_{J'J''} = \left[1 - A_1 J'' + A_2 J''^2 - A_3 J''^3\right]^2 \tag{6}$$

$$F^{Q}_{J'J''} = \left[1 + A_Q J''(J'' + 1)\right]^2 \tag{7}$$

Table 2
Hönl-London factors from [8]. These factors are only valid for $\Delta l = -1,\ 0,\ 1$.

Branch	$\Delta l = 0$	$\Delta l \neq 0$
P	$\frac{(J''+l''_2)(J''-l''_2)}{J''}$	$\frac{(J''-1-l''_2\Delta l)(J''-l''_2\Delta l)}{2J''}$
Q	$\frac{(2J'')l''^2_2}{J''(J''+1)}$	$\frac{(J''+1+l''_2\Delta l)(J''-l''_2\Delta l)(2J''+1)}{2J''(J''+1)}$
R	$\frac{(J''+1+l''_2)(J''+1-l''_2)}{J''+1}$	$\frac{(J''+2+l''_2\Delta l)(J''+1+l''_2\Delta l)}{2(J''+1)}$

$$F^{R}_{J'J''} = \left[1 + A_1 (J'' + 1) + A_2 (J'' + 1)^2 + A_3 (J'' + 1)^3\right]^2. \tag{8}$$

The Hönl-London factors and the ro-vibrational transition moments are fully determined through databases. However, the vibrational Einstein coefficients and the Herman-Wallis coefficients A_1, A_2, A_3 and A_Q are not included and need to be computed. It is worth mentioning that since the P and R branches share the same coefficients, the fitting should be done simultaneously for the two branches. Thus the least square fitting procedure is applied to the following equation:

$$A^{v'}_{v''} \times F_{J'J''} - \frac{A^{v'J'}_{v''J''}}{S^{l'J'}_{l''J''}} = 0. \tag{9}$$

Figs. 3 and 4 present examples of transition fitting using equation (9). Fig. 3 presents the fitting of transition 00011 → 00001 which has a P and R branch while Fig. 4 presents the fittings of transition 01111 → 01101. In both cases the fitting is able to match very well the data contained in CDSD4000. The reconstruction of these fits can be seen in Fig. 5 where data is used to reconstruct the ro-vibrational information contained in CDSD4000 and HITRAN. This reconstruction provides some validation of the fitting procedure ability to reconstruct the ro-vibrational information from vibrational specific data, as transitions 00011 → 00001 and 01111 → 01101 are reconstructed without any obvious flaws. The perturbations in the high rotational levels in the P and R branches are not reconstructed and when $J_{\max}$ is extrapolated these perturbations are not reproduced.

3.7. Transition database creation

Transitions in CDSD4000 are organized by their vibrational assignment excluding all the isotopes except the main one. The data associated to these transitions is used in the fit according to equation (9). Regarding the possible electric dipole transitions in CO_2 the ideal case would be the following procedure:

1. First case is only fitted once for P and R branches since no Q branch exists.
2. Second case is fitted once for P and R branches and another time for Q branch if l'_2 or l''_2 are equal to zero. If this is not the case, four fits must be performed: one for P and R with e symmetry, another for P and R with f symmetry, one Q with e and another Q with f.
3. Third case is always fitted four times as in the second case when both l_2 are greater than zero.

Some transitions have missing data or exhibit perturbations. Due to this missing/perturbed data, not all transitions can be successfully fitted. In a previous work [7], an attempt was done to develop a universal fitting approach. In this work, a different approach is considered where the data associated to transitions is analyzed and then classified into different categories. Thus, transitions are classified into a "usable" or "non-usable" categories depending on how much missing/perturbed data has been identified. Subjective merits such as the smoothness of the branches and the shape of the curves are used when classifying transitions as well.

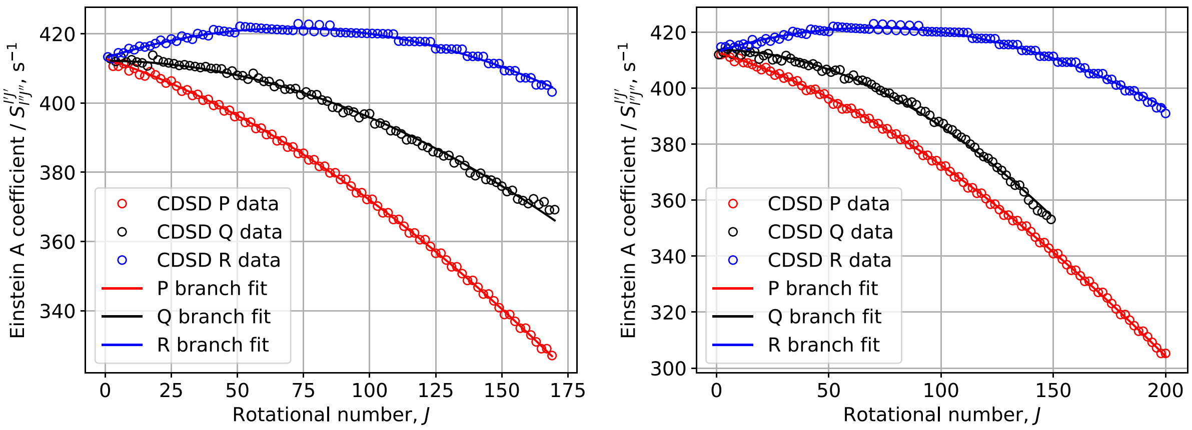

Fig. 4. Fitting example for transition 01111 → 01101. On the left, P and R branches with lower symmetry of e and Q branch with symmetry of f. On the right, P and R branches with lower symmetry of f and Q branch with symmetry of e.

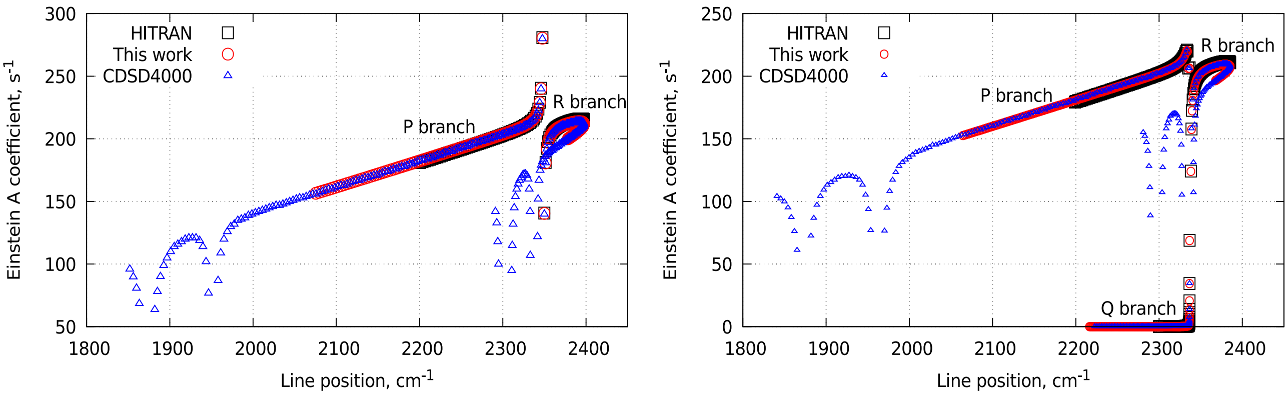

Fig. 5. Reconstruction examples for fitted quantities of transitions 00011 → 00001 (left) and 01111 → 01101 (right) compared against values from HITRAN and CDSD4000.

Table 3
Total number of cases considered for re-fitting divided by fit case and category.

Category	Case 1	Case 2	Case 3
Total	4146	111,843	88,863
Usable	761	1720	1772
Not Usable	2206	42,054	40,208
Too small	1179	68,070	46,883
Usable/Total(%)	18.0	1.5	2.0

Additionally, a category for transitions which do not have more than 20 points for P and R branches separately is used to ensure a minimum amount of data is available for the fit.

The number of vibrationally specific transitions, excluding unidentified transitions, is approximately 2.5 million. In order to reduce the considered dataset and as a first approach, only transitions with $\nu'_1 \le\le 4$ are considered. Table 3 presents the total number of transitions that meet the criterion $0 \le \nu'_1 \le 4$. The number of transitions in each category (“usable”, “non-usable”) after classification, as well as the percentage of usable transitions for each case, are listed in Table 3. Each column represents one of the cases for the possible electric dipole transitions for linear polyatomic molecules. Here we only consider transitions on the 4.3µm spectral region of the CO_2 spectrum. The resulting database is comprised by the upper and lower level assignments, Einstein coefficients, Herman-Wallis coefficients and the lower level Wang symmetry.

For some transitions the Q branch data is missing. If this is the case, the coefficient A_Q is considered to be zero. Convergence issues have been observed if A_3 is considered in the equations to be fitted. As such, A_3 was neglected and fitting only occurred with A_1, A_2 and A_Q. It was also found that filtering out perturbations and/or neglecting high rotational levels was required to obtain a good quality of the fits.

There is a way of reconsidering previously discarded transitions as well as including transitions outside the scope of the first classification process. A script was developed to compute the absorption for every ro-vibrational transition inside a specified spectral range in CDSD4000. By specifying a temperature and number density it returns a list of transitions which are above a specified threshold of absorption. This list can then be compared against the transitions in CDSDv and missing transitions can be (re-) considered for classification. This process may be iterated over different temperatures and spectral ranges to improve accuracy. It also includes transitions outside the previous criterion $0 \le \nu'_1 \le 4$.

Transitions that are reconsidered for classification will be classified again. In many cases it is impossible to fit these as the data does not have internal structure when seen through Eq. (9). In these cases it is not possible to fit any expression. These transitions may still be considered by averaging the RHS of Eq. (9) after the removal of outliers by the interquartile range method, while neglecting the influence of the Herman-Wallis factor:

$$A^{\nu'}_{\nu''} = \overline{\frac{A^{\nu'J'}_{\nu''J''}}{S^{l'J'}_{l''J''}}}. \tag{10}$$

With this averaging method, we are able to obtain a list of vibrational Einstein A coefficients. Databases such as CDSD and HITRAN use a cut-off criteria for ro-vibrational transitions, deciding which are included or discarded. Due to this cut-off criterion, the pro-

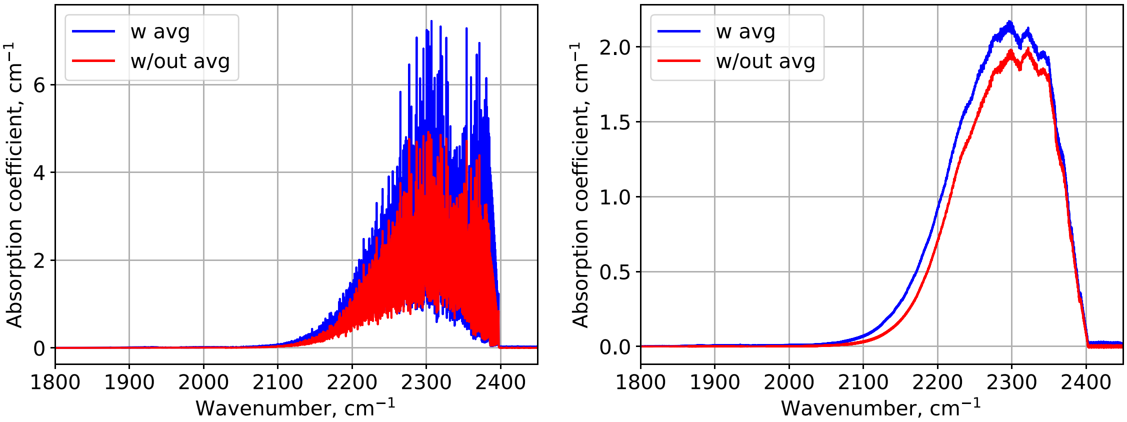

Fig. 6. Absorption coefficient for 1 atmosphere of pure CO_2 at 2000K of CDSDv with and without the Einstein coefficient averaging. The right figure is convoluted with a 10 cm^{-1} wide rectangular apparatus function.

posed averaging will overestimate the average of Einstein coefficients for a given transition. For now, only electric dipole transitions are included in the averaging process. Later on, transitions with $|\Delta l_2| > 1$ may be added to CDSDv however this falls outside the scope of this work. Fig. 6 presents the difference in the absorption coefficient between a simulation with and without Einstein coefficient averaging for 1 atm of pure CO_2 at 2000K with the exact lineshape on the left and the convolution with a 10 cm^{-1} wide square apparatus function on the right. There is a noticeable impact by including the averaged transitions in the database. This inclusion is necessary for better accuracy at higher temperature regimes. The results in this paper are obtained by retaining the averaged transitions in CDSDv.

4. Comparisons against other databases

4.1. Absorption coefficient

The absorption coefficient for 1 atmosphere of pure CO_2 was computed using CDSDv in the spectral range of 145 to 5500 cm^{-1} at 296, 1000, 2000 and 3000 K and compared with the results of SPECTRA [76] using HITEMP. The results are plotted in Fig. 7. The figures on the top present the results for the 296 and 1000 K case. In both figures, the peaks for the represented bands (left to right, 15, 4.3, 2.7 and 2.3 µm) are well matched as well as the wings of these bands, especially in the case of 1000K. The figures on the bottom present the results for the 2000 and 3000K case in which the absorption peaks are relatively well matched but CDSDv overestimates the inter-band region by several orders of magnitude. This is the consequence of transition averaging that was introduced in Section 3.7. Despite the overestimation in these regions, the relative magnitude of the radiative peaks in these regions is low when compared to the peaks located inside the spectral bands. At 2000K, this difference is up to 2 to 3 orders of magnitude in the worst case and is considered to be negligible. At 3000K the difference can be less than one order of magnitude and it's effect may no longer be considered to be negligible in some spectral regions. As a future update to the database, steps may be taken to ensure the averaging procedure does not overestimate the "global" radiative intensity for the averaged transitions.

4.2. Radiative power

The total radiative power of CDSDv is assessed by comparing the contribution of CO_2 IR radiation for an equilibrium Martian-like 97% CO_2 - 3%N_2 mixture to other authors. This comparison is shown in Fig. 8. The full lines are the contribution of CO_2 IR radiation to the total radiative power by Lino da Silva [26] in grey, by Perrin et al. [43] in red and CDSDv in blue. The dashed lines in black and red are the contribution of other systems relevant to the CO_2-N_2 mixture. The three calculations of the contribution of CO_2 radiative power are in reasonable agreement. CDSDv slightly underpredicts both results from Lino da Silva and Perrin et al., although the latter seems to approximate CDSDv on the low and high temperature limits of the calculation.

4.3. Performance

The performance of the CDSDv database was assessed by using an in-house tool for the calculation of the emission and absorption spectra from the Dirac properties of radiative lines as described in [57] and in Section 3.2. The same calculation was also performed using the CDSD4000 database. In summary the process in [57] sorts lines into "strong" and "weak" categories. Strong lines are checked for coverage of other strong lines and processed by explicitly computing the Voigt lineshape (if they are uncovered by other lines). Weak lines are treated as pseudo-continuum. Performance largely depends on the distribution and number of strong lines. Results for this calculation are summarized in Table 4. Each set of results is one of four possible combinations between tight and lax numerical parameters and a spectral range of 2000–2500 or 2100–2500 cm^{-1}. Tight and lax parameters refer only to the threshold below which lines are considered weak and above are considered strong. In each combination of parameters and spectral range the radiation of 1 atmosphere of pure CO_2 is simulated at 1000, 2000 and 3000K corresponding to Time 1, 2 and 3 respectively. Also presented are the maximum RAM (Random-access Memory) used in each simulation and the input file size. In Fig. 9 the ratios of calculation times and the ratio of strong lines between CDSD4000 and CDSDv is plotted. Although this is not an extensive performance test there are some trends that might be suggestive of the general relative behaviour of both databases. The first trend is that increasing temperature decreases relative performance but always maintains it above one. At low temperatures the performance difference is mostly impacted by the calculation of the pseudo-continuum. CDSD4000 with approximately 81 million lines will underperform when compared to the 5 million lines in CDSDv. At higher temperatures the calculation time is dominated by the number of strong lines that need to be treated. In tests 2 and 3 the ratio of strong lines can be between 1.1 and 1.5 as shown in fig 9 which leads to performances usually below a factor of 2 better between CDSD4000 and CDSDv. The second trend is that increasing the spectral range and retaining lax numerical parameters leads to better performance of CDSDv. In a small spectral range the

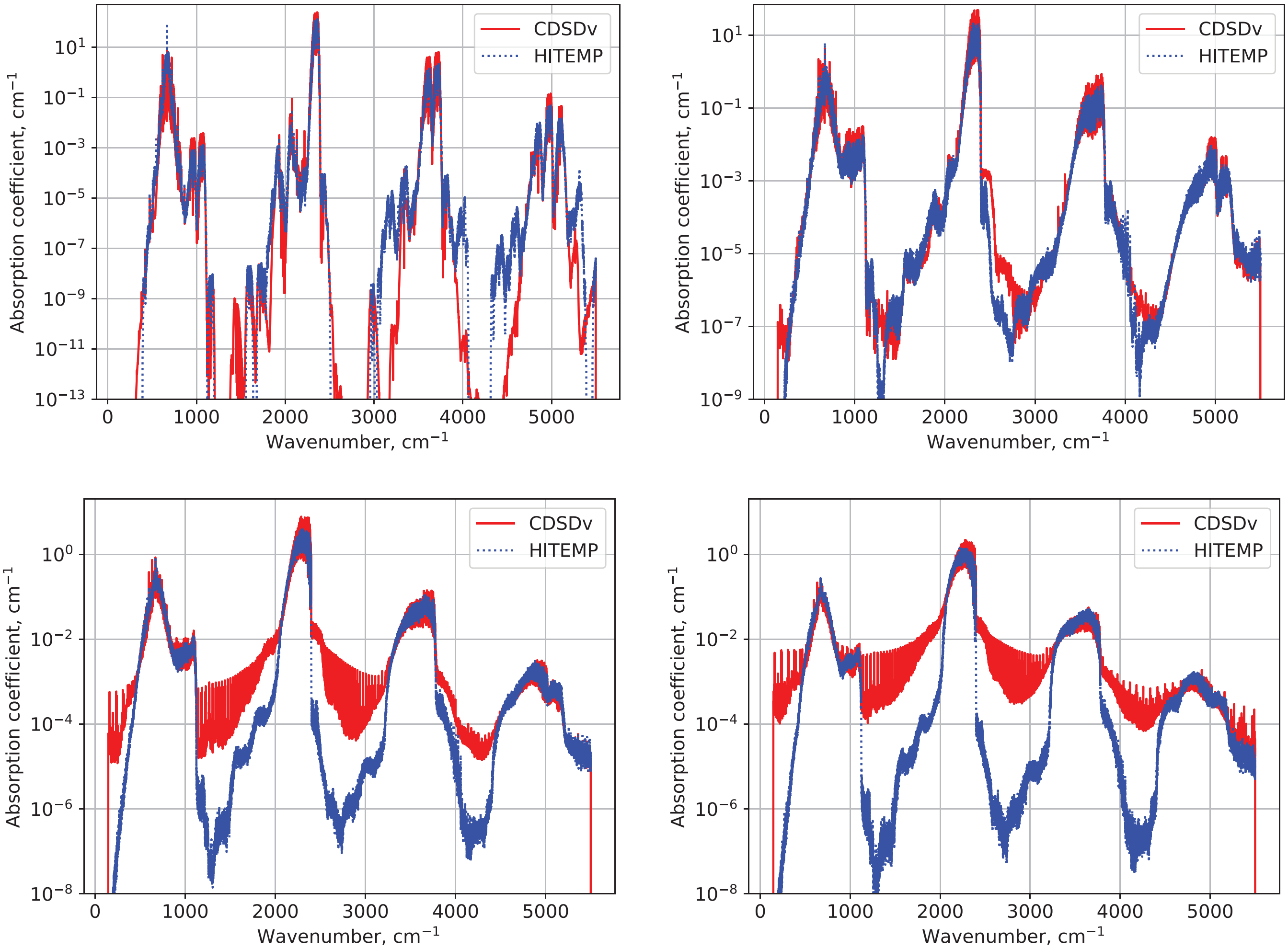

Fig. 7. Absorption coefficient for 1 atmosphere of pure CO_2 between 145 to 5500 cm^{-1} at 296 (top left), 1000 (top right), 2000 (bottom left) and 3000K (bottom right) using databases and tools for interpreting CDSDv and the online tool SPECTRA using HITEMP.

Table 4
Performance of CDSD4000 and CDSDv using the method of described in [57] using tight or lax numerical parameters in a spectral range of 2100–2500 or 2000–2500 cm^{-1}.

#	Parameters	Range (cm^{-1})	Database	Time 1 (s)	Time 2 (s)	Time 3 (s)	Max RAM	# Lines
1	Tight	2100–2500	CDSDv	30.98	329.58	2855.43	446.3 MiB	4,266,280
			CDSD4000	85.18	356.25	3891.64	3.830 GiB	37,497,133
2	Lax	2000–2500	CDSDv	20.11	145.11	1007.92	607.75 MiB	5,867,324
			CDSD4000	174.95	341.63	1773.45	7.985 GiB	81,963,950
3	Lax	2100–2500	CDSDv	17.09	124.82	613.40	442.7 MiB	4,266,280
			CDSD4000	65.53	183.89	791.06	3.660 GiB	37,497,133
4	Tight	2000–2500	CDSDv	39.95	574.38	6846.50	608.14 MiB	5,867,324
			CDSD4000	181.62	738.41	12253.16	7.963 GiB	81,963,950

number of strong lines in CDSD4000 and CDSDv will be approximately the same. With a greater spectral range and sufficiently relaxed numerical parameters, (while maintaining safe margins for faithful reproduction of the exact spectrum) a better global performance might be achieved. Something worth mentioning and not shown by this performance check is that it would be impossible to simulate a full spectrum of CDSD4000 with the available computational resources as is done in Fig. 7. This can be done with CDSDv and at least in a smaller spectral range, CDSDv is always faster than CDSD4000.

One last comparison was performed where the pseudo-continuum method is not used. The purpose of this test is to make a direct comparison of the number of lines used in CDSD4000 and CDSDv and the computational times using the same thresholds but without any numerical shortcut. In these simulations any line with absorption and emission 10^5 times smaller than the highest absorption and emission of the entire ensemble of lines is discarded. The temperatures 1000, 2000 and 3000K are again considered in the spectral range of 2000–2500 cm^{-1}. The results for this calculation are presented in Table 5. The total number of lines in this spectral region are 5,823,586 for CDSDv and 81,963,950 for CDSD4000. Only a fraction of the total number of lines are used in these calculations. At 1000K both databases use a similar number of lines. CDSD4000 takes 63 seconds compared with the 23

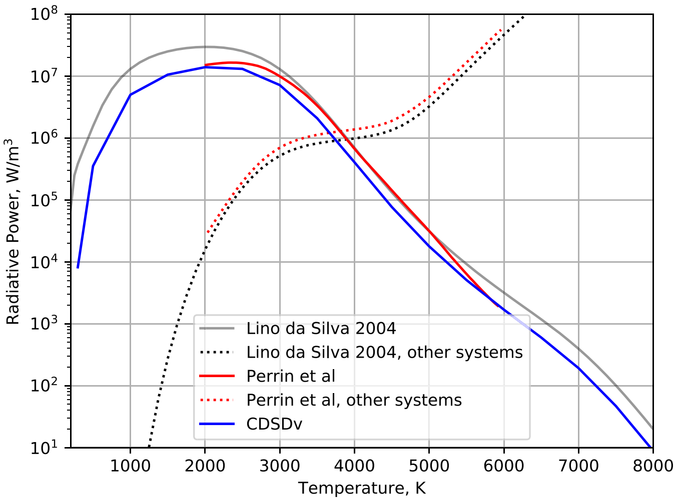

Fig. 8. Radiative Power for an equilibrium Martian-like 97% CO_2 - 3% N_2 mixture. The full lines present the radiative power from IR CO_2 while the dashed lines present the radiative power from other radiative systems relevant to CO_2-N_2 mixture. Data from Lino da Silva in [26], data of EM2C from [43].

Table 5
Performance comparison between CDSDv and CDSD4000 for the calculation of 1 atmosphere of pure CO_2 at 1000, 2000 and 3000K. The computational time is proportional to the number of lines considered for the calculation.

	Time (s)		Number of lines	
Temperature	CDSDv	CDSD4000	CDSDv	CDSD4000
1000 K	23	63	35,314	35,832
2000 K	445	504	565,066	662,118
3000 K	1997	2873	2,230,224	3,416,204

Table 6
Test cases in Lemal et al. [77].

Label	T (K)	p (atm)	x (%)	L (cm)	Δ (cm^{-1})
a	500	1	100	54	30
b	1000	1	100	50	30
c	1203	1	43	54	40
d	1300	1	100	50	35
e	1550	1	50	50	10
f	1770	1	18	54	30
g	298	1	100	95.3	10
h	500	1	100	53.3	15
i	1000	1	5	40	15
j	1300	1	100	40	10
k	1500	1	100	7.75	25
l	300	0.66	6	5.14	50
m	667	0.5	11	9.64	10
n	1000	1	100	50	12
o	1200	1	100	7.75	30
p	1300	1	100	50	50
q	1500	1	53	7.75	10
r	1771	1	17	54	54
s	2850	1	24	2.34	20
t	500	1	100	53.4	7
u	1000	1	100	50	6
v	1203	1	43	53.7	3
w	1473	1	1	50	5
x	1950	1	53	3.12	5
y	2300	1	49	1.67	5

seconds of CDSDv due to the time it takes to read the input file of CDSD4000. At 2000K the calculation using CDSD4000 takes almost a minute longer than CDSDv due to the overhead from reading a much larger input file and handling 100,000 more lines in the calculation. At the highest temperature, CDSD4000 takes approximately 45 minutes compared against the 30 minutes of CDSDv. The difference in the number of lines is also very significant with 2.2M considered by CDSDv and 3.4M considered by CDSD4000. Obviously, this comparison is inconsequential if the obtained spectra are too different. Fig. 10 presents the absorption coefficient obtained from the calculations of 1 atmosphere of pure CO_2 at 1000, 2000 and 3000K as in Table 5. The absorption coefficients were convolved with a 10 cm^{-1} rectangular apparatus function. For the 1000 and 2000K cases, the obtained spectra are quite similar but in the 3000K case there are significant differences between the CDSD4000 and CDSDv absorption coefficients. This is not necessarily a deal breaker, as the pressure and the typical dimension of the system also come into play in determining how important radiative heating will be at this temperature. In the next section, applications of CDSD4000 in the literature are reviewed and compared against CDSDv.

5. Comparisons against experimental data

5.1. Transmittance

The transmittance of CDSDv was computed according to the test cases presented in [77] which include simulations using CDSD4000 and experimental measurements. The conditions used for these simulations are summarized in Table 6 where the lettered labels are the same as in [77]. The number density in each case may be determined by $N = xp/k_BT$ where x is the fraction of CO_2. The transmittance τ is computed for a length L through:

$$\tau_{\overline{\nu}} = \exp\left(-\alpha_{\overline{\nu}} L\right) \tag{11}$$

where $\alpha_{\overline{\nu}}$ is the absorption coefficient at position $\overline{\nu}$. The quantity Δ is defined in [77] as the spectral resolution which by itself is poorly defined in this context. In this work it was taken as a moving average window for post-processing of the exact result. The results for these simulations can be seen in Figs. 11–14 for the 2.3, 2.7, 4.3 and 15 µm regions respectively. Most cases are well matched with experiments and/or calculations. Two cases stand out as almost or completely mismatched with either experiments or calculations, case b) and s).

Case b) is in the 2.3 µm region shown in Fig. 11. In this region, CDSD4000 does not perform particularly well against experimental values. For instance the region between 5000–5200 cm^{-1} is completely missed. It is not surprising therefore to see a case where refitted transitions from CDSD4000 do not perform well. It is surprising that the 5000–5200 cm^{-1} region is captured relatively well by CDSDv in most cases. This might be purely coincidental as beneficial result of extrapolations of CDSDv beyond the cutoff parameter of CDSD4000 (since it is the lineshape routine which adoptively manages these, instead of the databases). The region between 4600–5000 cm^{-1} is also generally well captured, close to experiments and calculations except in case d) where it is close to calculations but far from the experimental points.

In the 2.7 µm region, (Fig. 12) CDSDv performs very well against experiments and calculations except in case i) where the absorption coefficient is underestimated and thus, the transmittance is overestimated.

The 4.3 µm region, shown in Fig. 13, displays also the other worst case, s). Here, the gas temperature is already high enough (2850 K) and the gas dimension small enough that any initial discrepancy is enhanced as per Eq. (11). The absorption has to be very well estimated to capture the region where $0 < \tau_{\overline{\nu}} < 1$ as it happens in case s) where transmittance is between 0.2 and 0.8 in the region of $2050 - 2375$ cm^{-1}. All other cases are close to experimental calculations and experimental measurements except case l) where most points between 2300–2475 cm^{-1} are closer to the CDSDv line than CDSD4000.

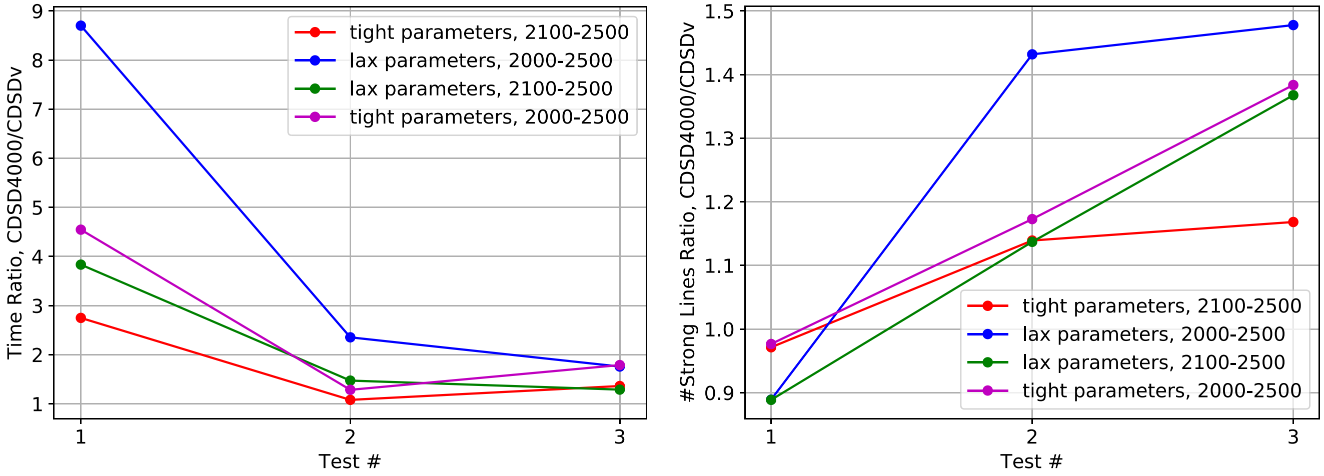

Fig. 9. Ratio of simulation times (on the left) and ratio of number of strong lines between CDSD4000 and CDSDv for each case in Table 4.

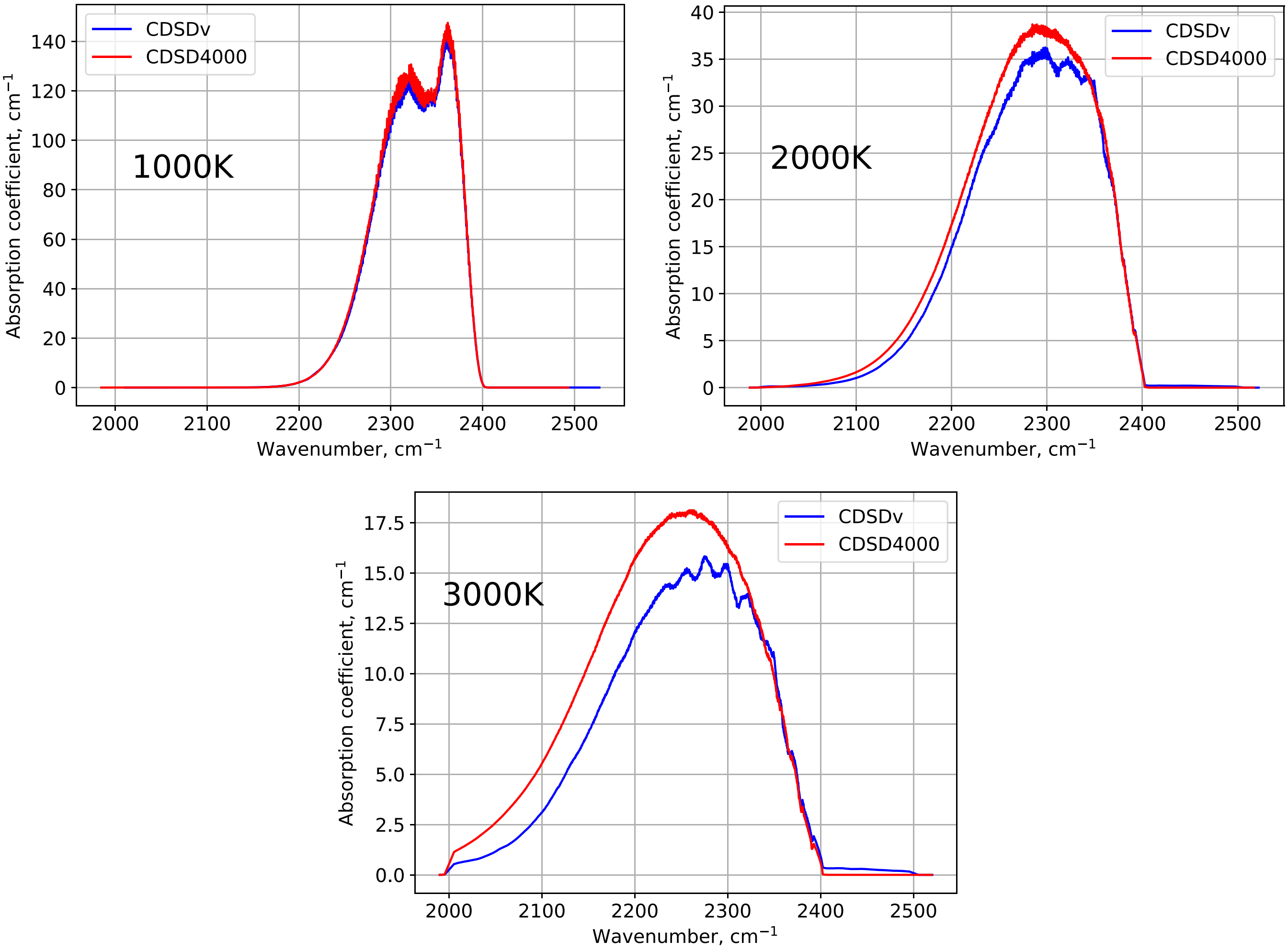

Fig. 10. Absorption coefficients for 1 atmosphere of pure CO_2 at 1000, 2000 and 3000K computed with CDSD4000 and CDSDv. These results were convoluted with a 10 cm^{-1} wide rectangular apparatus function.

The last spectral region treated in this work, 15 μm is shown in Fig. 14. In these cases CDSDv fares as well as or better than CDSD4000 as in cases w), x) and y). The reason for this might be that calculations with CDSD4000 are usually performed with the Lorentzian HWHM coefficients present in the database. These coefficients only account for self-broadening and/or air-broadening. CDSDv does not assume any coefficients for Lorentz broadening relying instead on general expressions that account for different collisional effects, including different mixtures than the ones used in CDSD4000. Cases w), x) and y) are cases where the gas mixture is not fully composed of CO_2 and therefore, Lorentz broadening cannot be fully accounted using self-broadening only as it is usually done in CDSD4000.

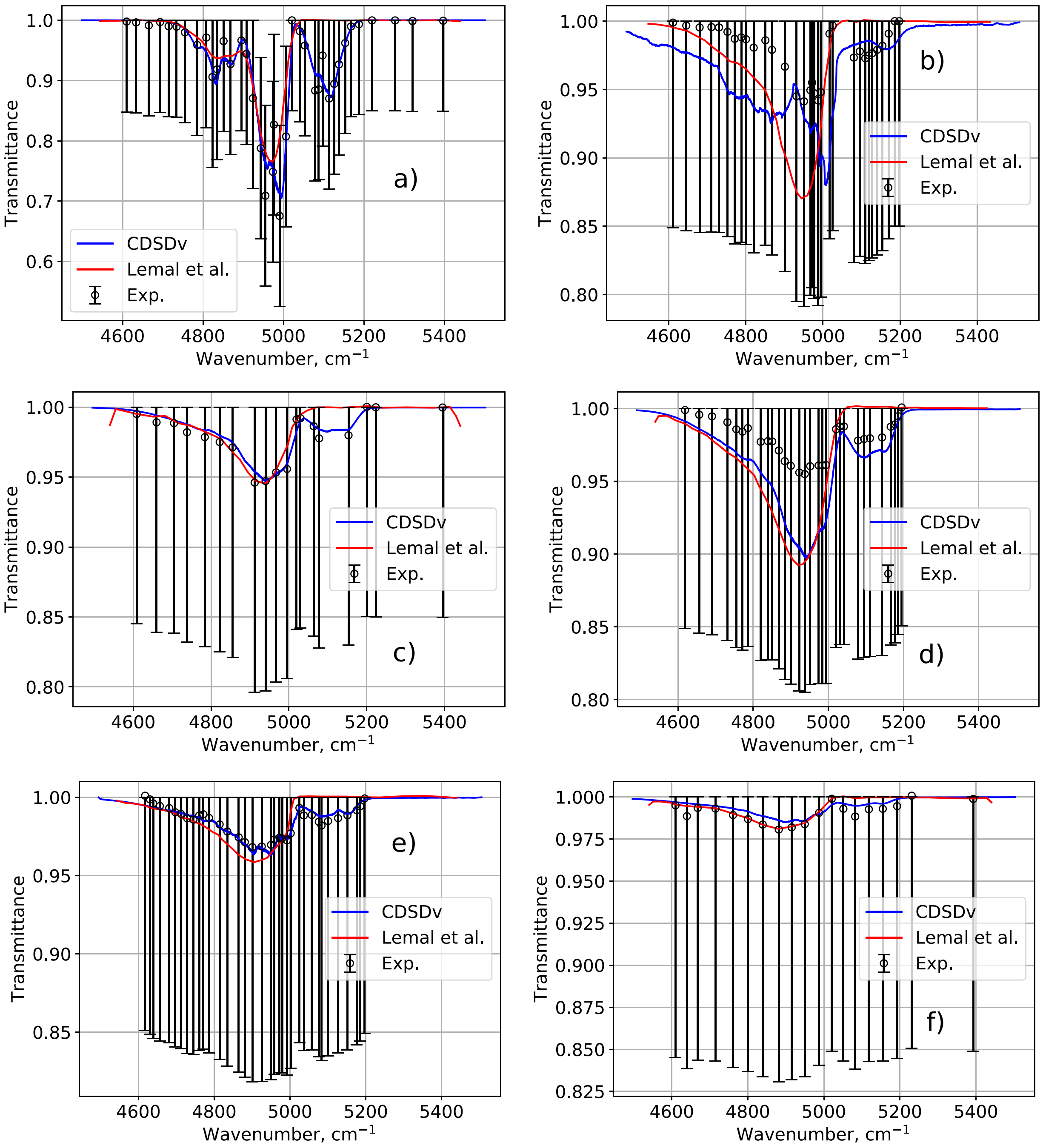

Fig. 11. Transmittances for test cases listed in Table 6 compared against the same listed in [77] for the 2.3 μm region, cases a through f.

5.2. JAXA Mars entry condition

Measurements of IR radiation of CO_2 were performed out in JAXA expansion and shock tube facilities and reported in [79]. Pannier and Laux carried out a numerical and radiative analysis using the code RADIS [80] and the CDSD4000 database [78]. Fig. 15 displays the framework for the calculations carried out in [78]. The line of sight is composed of three cells. The first and the last have the same size and gas conditions. Part of the work developed by Pannier and Laux was to assess which conditions in the three cells would make a better match for the experimental measurements. The first and last cells would be considered "freeflow" cells characterized by low pressure and non-equilibrium. The freeflow conditions were estimated by measurements performed with the line of sight blocked by the model in the expansion tube. The conditions in the freeflow were then determined to be: $T_{CO} = T_{CO2} = 2200K$ and $T_{gas} = T_{rot} = 1690K$ at a pressure of 17 mbar with the molar fraction of CO_2 being 0.606 and CO 0.257. The center cell would be the "forebody" region chracterized by a high-pressure shock wave, thermal equilibrium and strong dissociation of CO_2. With the free-stream conditions fixed, the center cell is considered to be at $T = 4000K$ with a pressure of 1 bar. CO_2 is mostly dissociated amounting to only 0.027 molar fraction and CO corresponds to 0.520 molar fraction. The radiance is computed through the radiative transfer equation:

$$L_n^{\nu} = \frac{\epsilon_n}{\alpha_n}(1 - \exp(-\alpha_n d)) + L_{n-1}^{\nu} \exp(-\alpha_n d) \tag{12}$$

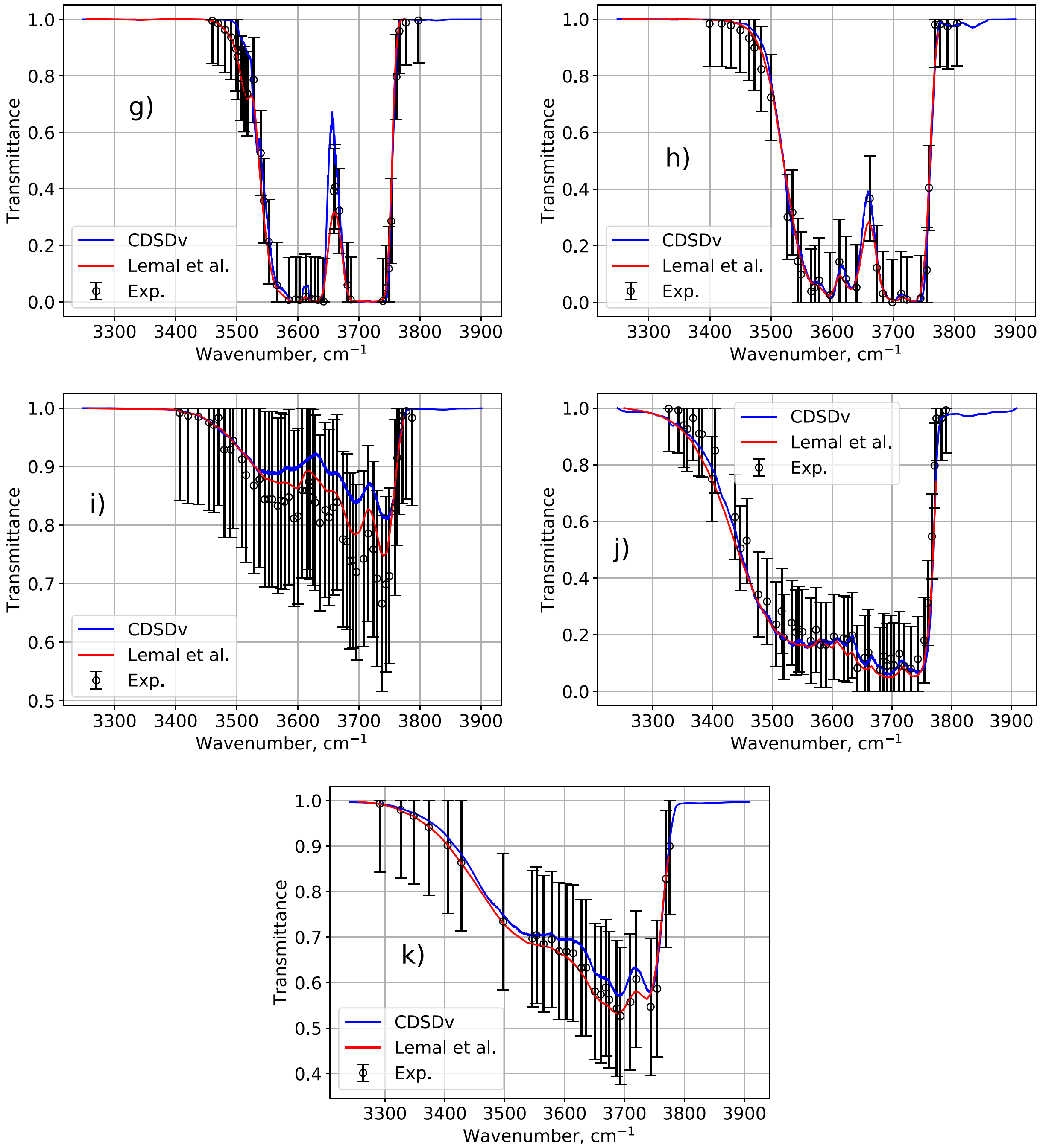

Fig. 12. Transmittances for test cases listed in Table 6 compared against the same listed in [77] for the 2.7µm region, cases g through k.

where ϵ_n is the emission coefficient and α_n the absorption coefficient in the n-th cell and d is the length of the cell. The absorption coefficient calculated with CDSDv already includes a self-absorption correction. Fig 16 shows the best case result presented in [78] and briefly described in this paragraph. It also displays the same case computed with CDSDv and our in-house radiation code (SPARK line-by-line). The experimental and numerical results are reproduced quite well by CDSDv. There is a small underprediction in the tail region between 4600–4900 nm. According to the analysis carried out in [78] CO is the main radiator in this region and a detailed comparison showed that out database describing CO IR radiation might need an update. In the cases described in this work however focus will be on CO_2 radiation and as such, an update on the CO database will be left for future work.

5.3. EAST Shock tube - MSL conditions

A shock tube experimental campaign was performed in the Electric Arc Shock Tube (EAST) facility in NASA Ames Research Center to replicate the conditions experienced by the Mars Science Laboratory (MSL) which landed on Mars in 2012. These series of tests are known as EAST test suite 55. A work analysing the radiative heating experienced by MSL during atmospheric entry was published by [2] which uses data from the aforementioned campaign to explain the measurements obtained by the MSL thermocouples embedded in the heat-shield. Data was taken from this campaign from the conditions which most resemble the peak radiative heating, shots 9 and shot 30 and additionally shot 19 is also considered in this work as a low pressure case the radiative signal

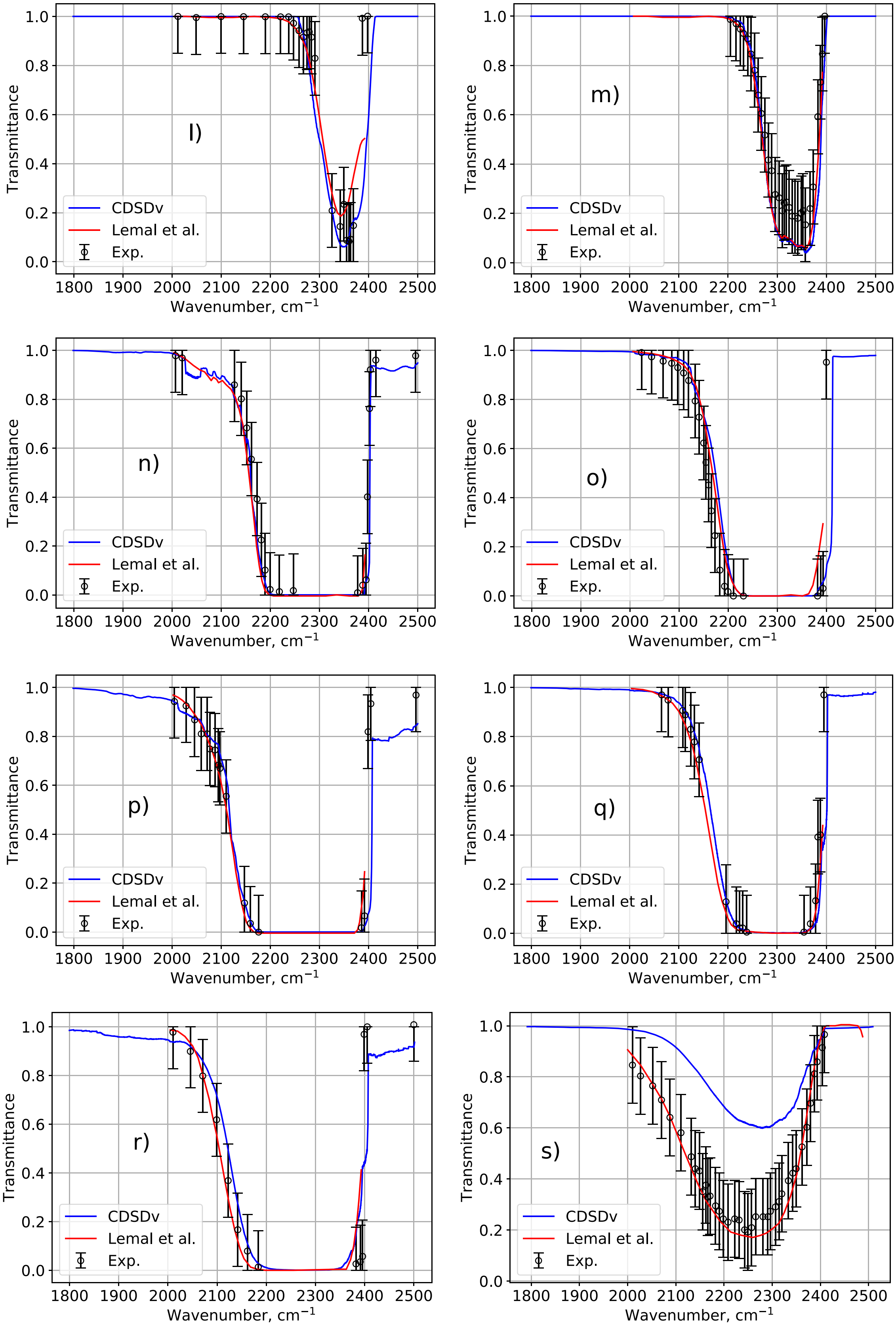

Fig. 13. Transmittances for test cases listed in Table 6 compared against the same listed in [77] for the 4.3 µm region, cases l through s.

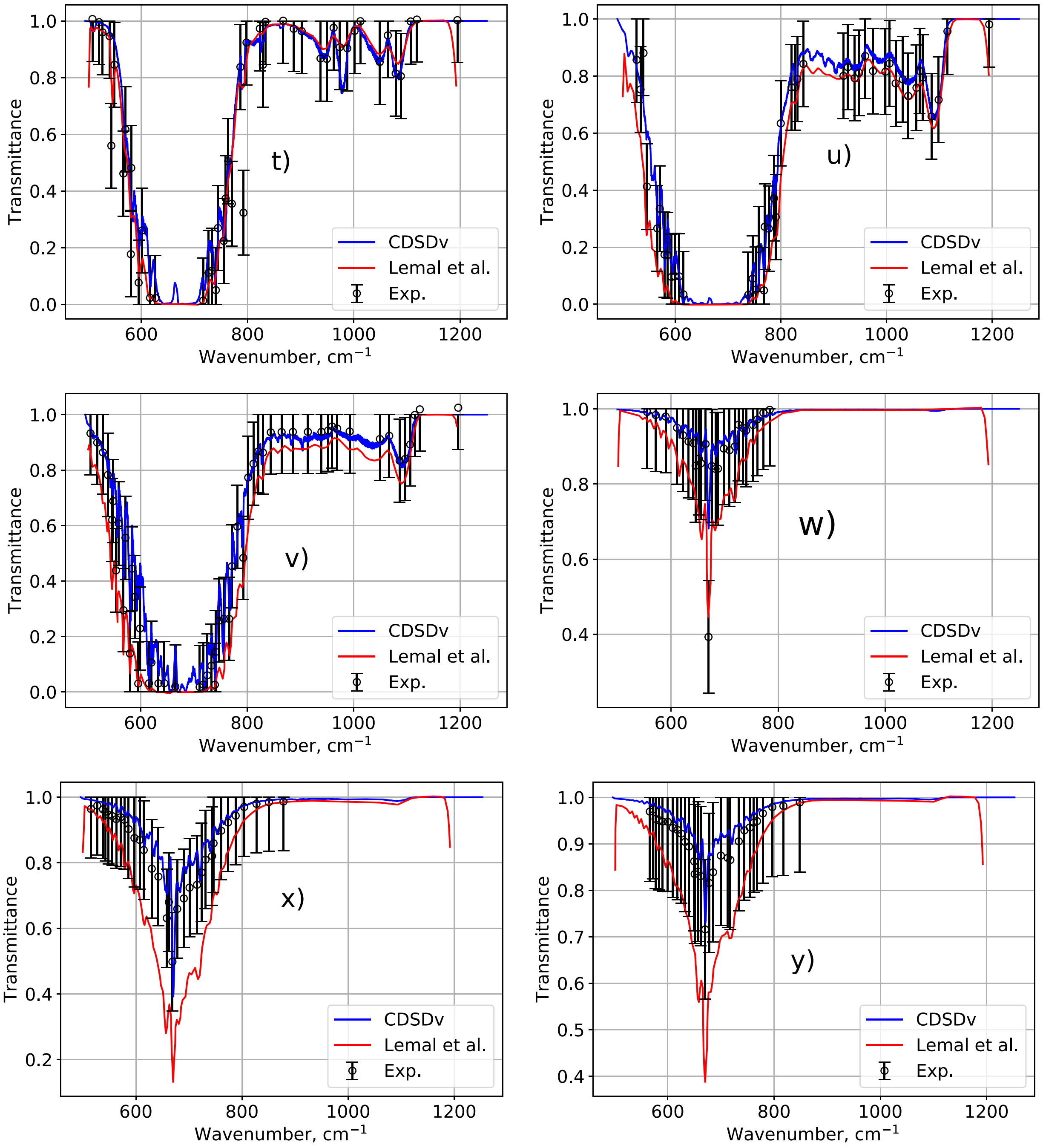

Fig. 14. Transmittances for test cases listed in Table 6 compared against the same listed in [77] for the 15 µm region, cases t through y.

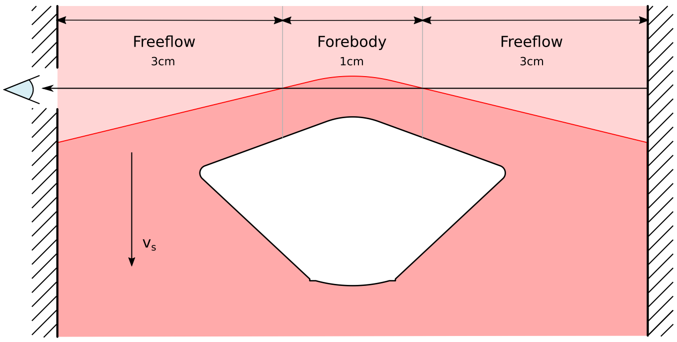

Fig. 15. Schematic for the calculation performed in [78] to reproduce the results in [79].

of two different kinetic models. Table 7 presents the conditions inside the shock tube for each considered shot.

In the low pressure case (shot 19), using the in-house code SPARK, the 1D shock relaxation is solved using Park's kinetic scheme described in [81] or Cruden's kinetic scheme described in [82]. Park's kinetic scheme does not consider `Ar` and Cruden's kinetic scheme does not consider `Ar` and $\mathtt{N}_2$ and as such these species were neglected in their respective simulations. From the 1D relaxation, the pressure, molar fractions, vibrational temperatures (shared by $\mathtt{CO}_2$ and `CO`) and gas temperatures are obtained and the radiance of the flow is obtained considering a 10.16 cm tube (EAST dimensions). Eq. (12) is used to compute the radiance without the additional term on the right hand side of the equation. Fig. 17 presents the measured and calculated radiance us-

Table 7
Conditions and measured spectral region in EAST for shots 9, 19 and 30 of test 55. The molar composition is the same for all shots and all were performed at ambient temperature.

Shot #	Pressure (Torr)	Shock s peed (km/s)	Spectral Region (µm)	Molar composition
9	1.0	3.69	4.3	95.8% CO_2
19	0.1	5.52	4.3	2.7% N_2
30	1.0	3.64	2.7	1.5% Ar

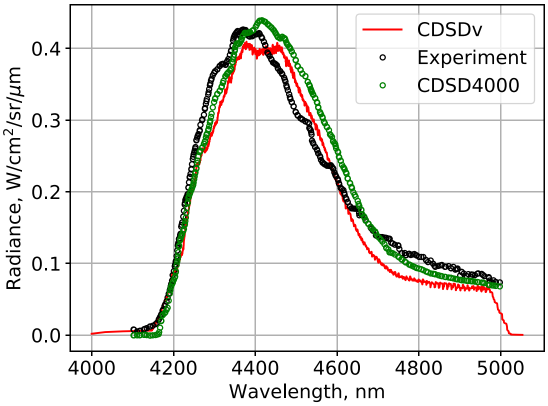

Fig. 16. Measurement and calculation of radiance in the shocked flow around a model of a spacecraft. Experiments were carried out by [79] and the calculation using CDSD4000 by [78]. The calculation using CDSDv was performed for this work.

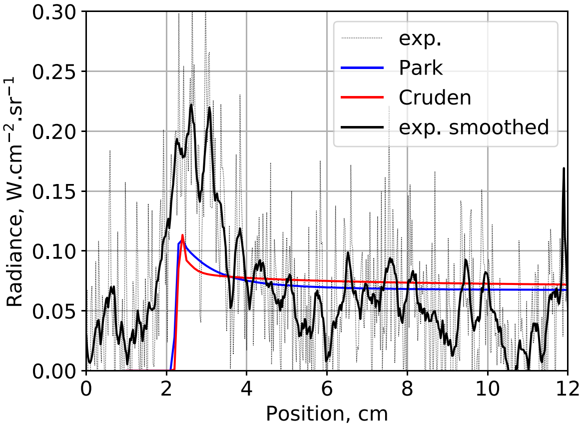

Fig. 17. Measurements and calculations of the radiance for a shock-wave of a 0.1 Torr gas with a composition of 0.958 CO_2, 0.027 N_2, 0.015 Ar at 5.52 km/s.

ing Park and Cruden kinetic models. The measured radiance was smoothed out for aiding in visualization. The radiative signals from Park and Cruden models are very similar for this shot. Both peak at the same position and relax in comparable time scales. The post-shock tail is also very close two centimeters after the shock. While not completely in equilibrium in the measured distance after the shock, there is a small difference in the equilibrium parameters due to the inclusion of N_2 in Park's model. The experimental peak is approximately twice the calculated peaks.

In the high-pressure case, using an equivalent stagnation line profile for the flow, kindly ceded by B. Cruden, the aforementioned treatment is applied with Eq. (12). Instead of the ideal 1D post-shock flow, the equivalent stagnation line accounts for diffusion effects across the shock-wave as described in [83]. In Fig. 18 the measured and calculated radiance of shots 9 and 30 are plotted. Shot 9 was measured in the 4.3 µm region and shot 30 in the 2.7 µm region. The simulated shot 9 is in very good agreement with the experimental results, the abrupt end in calculated signal at the end is due to an early stop in the simulation. On the 2.7 µm region there is no agreement with the experimental values and the signal is not simulated fully along the test distance. The mismatch between experiments and simulations in this spectral region is attributed to missing transition data in the 2.7 µm region of CDSDv.

5.4. Atmospheric plasma torch

In the work of Depraz et al. published in two parts [84,85], an high-temperature CO_2 microwave plasma is studied and characterized. The radiance of the plasma was measured at a height *h* of 6 and 20 mm and also at different distances from the central chord of the plasma. These measurements are compared with

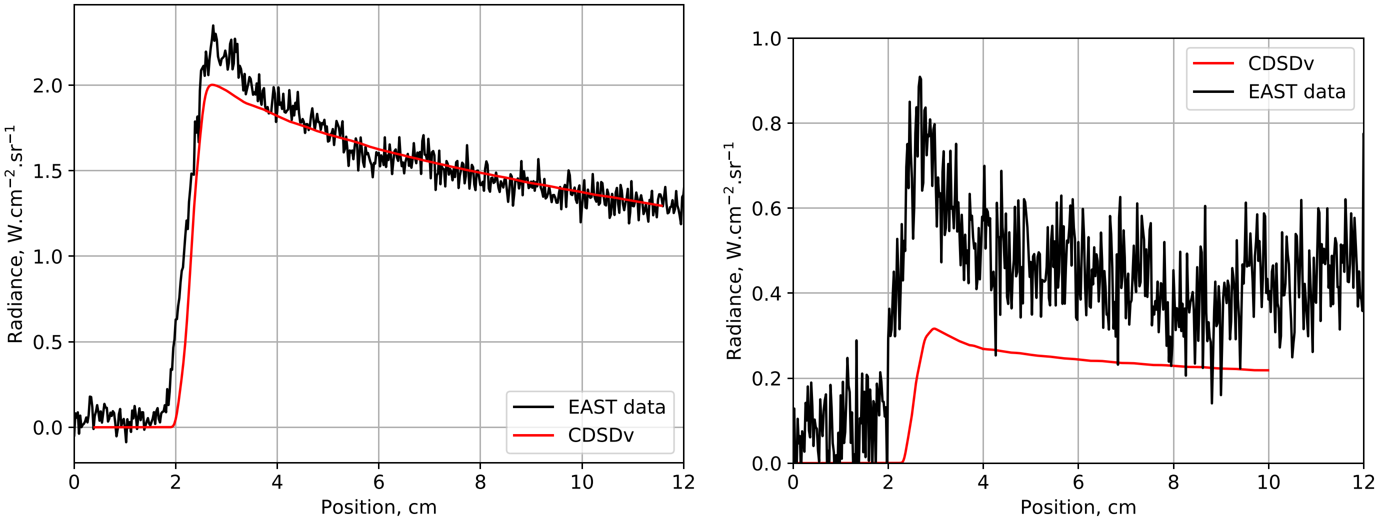

Fig. 18. Measurements and calculations of the radiance for a shock-wave of a 1 Torr gas with a composition of 0.958 CO_2, 0.027 N_2, 0.015 Ar at 3.69 km/s in the 4.3 µm region (left) and 3.64 km/s (right) in the 2.7 µm region.

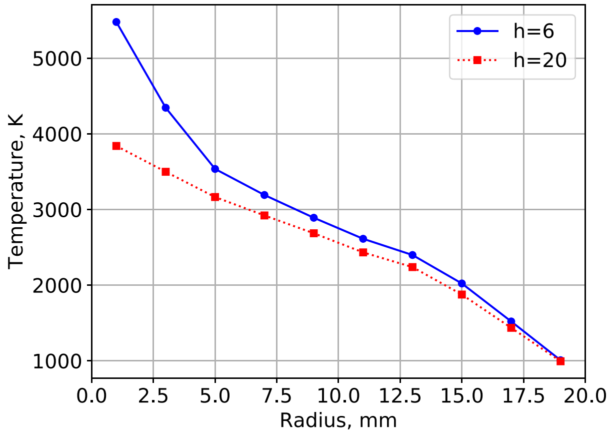

Fig. 19. Temperature and molar fraction profiles for the cases where $h = 6$ mm and $h = 20$ mm in the atmospheric plasma torch experiment in [84] and [85].

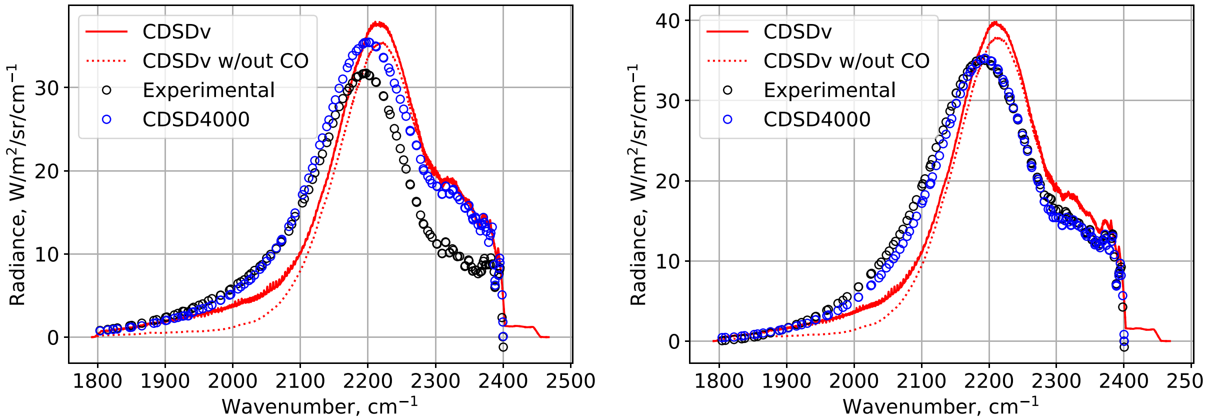

Fig. 20. Measurements and calculations of the radiance of the atmospheric plasma torch in the 4.3 μm region at a $h = 6$ mm (left) and $h = 20$ mm (right). Calculations were performed using CDSD4000 and CDSDv.

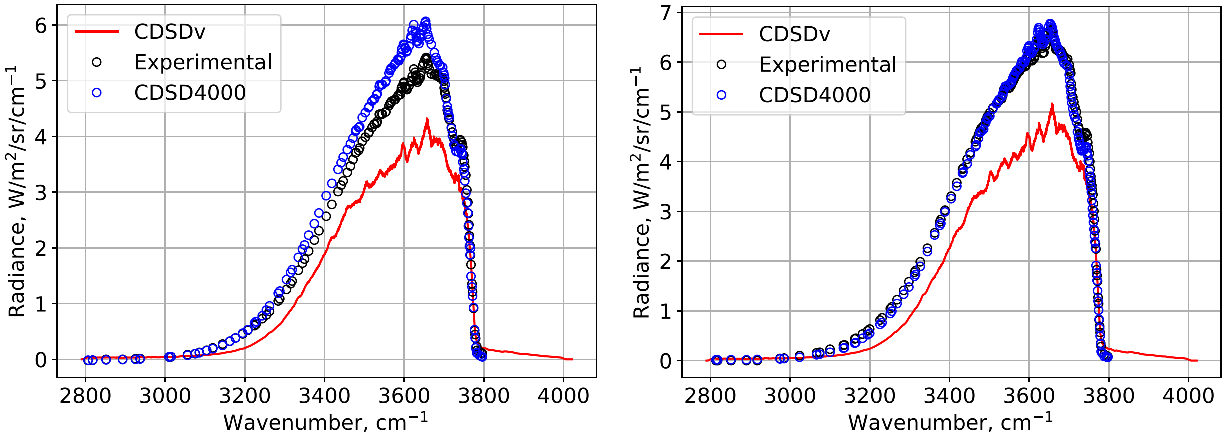

Fig. 21. Measurements and calculations of the radiance of the atmospheric plasma torch in the 2.7 μm region at a $h = 6$ mm (left) and $h = 20$ mm (right). Calculations were performed using CDSD4000 and CDSDv.

calculations using CDSD4000. In this work we will focus on the measurements taken at different heights in the central chord. Fig. 19 presents the radial profile of the plasma torch. The continuous profile was divided in ten cells and its conditions averaged to yield the discrete profile in Fig. 19. For this calculation the full diameter profile is taken, with the two cells closest to the center merged, according to the line of sight. Again, Eq. (12) is used along the line of sight with the self-absorption correction.

Fig. 20 presents the results for the 4.3 μm region at the two heights, 6 (left) and 20 (right) mm. In this spectral region calculations were performed including and excluding the radiation from `CO`. By including `CO` there is a non-negligible effect in the region 1200 – 2250 cm^{-1}. Most notably, the radiative peak is higher and the region 1800 – 2050 is closer to experimental lines than the calculation without `CO`. CDSDv curves in the 2250 – 2400 cm^{-1} region are matching CDSD4000 quite well at $h = 6$ but fail otherwise. The radiative peak, while close in magnitude, is blue shifted by a bit less than 20 cm^{-1}. Both databases overestimate the experimental measurements in the 2150 – 2400 cm^{-1} region. At $h = 20$ mm, the analysis is similar, except the 2150 – 2400 cm^{-1} region is well predicted by CDSD4000 and overestimated by CDSDv. The peak is still blue shifted by a similar value as in the $h = 6$ measurement.

Fig. 21 shows the results for the 2.7 µm spectral region. The figure on the left is the measurement and calculation corresponding to $h = 6$ mm and the figure on the right to $h = 20$ mm. In this region CDSDv underestimates the experimental and calculated results in the work of Depraz et al. The inclusion of $\mathtt{CO}$ in this region does not change the radiative profile significantly and is therefore deemed negligible.

The underestimation in the 2.7 µm region is attributed to transition data missing from CDSDv. A review of this spectral region might improve the results for a better match with experimental results. In the 4.3 µm region, where most time was devoted to the construction of CDSDv, the situation is more complex. Although there might be some missing information in the $1900 - 2150$ cm^{-1} region, there might also be an issue with the refitting procedure carried out during this work. A better translation of the data contained in CDSD4000 (in refitting and averaging procedures) is possible and it could improve results to the point where a better match with CDSD4000 calculations would be achieved.

6. Conclusions

We have presented a method for refitting ro-vibrationally specific radiative databases in the format of HITRAN, HITEMP, and CDSD to vibrationally specific. We have applied this method to the refitting of CDSD4000 and have branded the resulting database CDSDv. The use of these compact databases carries several advantages over the original ones:

- Both level and transition databases fit in an email attachment, two binary files 10.6 MB in total, 16.6 MB in ASCII format.
- The total number of ro-vibrational lines is greatly reduced in the main spectral regions of interest. For example, in the 4.3 µm region, the 81 million lines from CDSD4000 are reduced to 5 million lines in CDSDv.
- Possibility to separate vibrational and rotational modes with individual temperatures.
- This reduced number of lines leads to lesser computational overheads, namely regarding memory and processing power. While a full spectrum comparison could not be carried out in this work, due to the large size of CDSD4000, a standard laptop is able to simulate a full high-temperature $\mathtt{CO}_2$ infrared spectra in a reasonable time, using CDSDv.
- Several experimental and calculated results were adequately reproduced by CDSDv which may therefore be considered experimentally validated.

Naturally, a few disadvantages also exist:

- The reordering of the CDSD database from frequency-based to quantum transition based may in some cases be a disadvantage, such as in atmospheric sensing applications, where only a specific spectral window is of importance
- In addition to the loss of accuracy already mentioned, it is not possible to account for perturbations in the spectra using our method.

Owing to the aforementioned points, CDSDv is a database appropriate for the calculation of high-temperature, broadband $\mathtt{CO}_2$ radiation, such as in the case of Mars atmospheric entries. In some cases it exceeds the performance of CDSD4000, which can be attributed to the more generic methods applied for the calculation of Lorentz broadening, whereas CDSD4000 is more limited in the gas mixtures selection, as regarding broadening mechanisms. In trying to reproduce other results, CDSDv sometimes failed to achieve an excellent match. Most notably, cases where $\mathtt{CO}_2$ can be found at a relatively high-temperature are not always well reproduced by CDSDv. These results may be improved by reworking the averaging procedure, the refitting procedure in some circumstances and by including more transition data in regions where these might be lacking. As an example, preliminary tests have shown that extending the expressions for the Hermann–Wallis coefficients, namely adding a reciprocal term in Eqs. 6–8 (in the form of C/J where C is a fit parameter), may bring a non-negligible number of bands currently considered to be unfitable back in the fitable range. All of these changes will be postponed to a future version of CDSDv. The current version of CDSDv, is nevertheless considered mature enough to be of use to the community.

CDSDv is part of the libre code SPARK line-by-line. Both can be handed upon request [86].

Declaration of Competing Interest

The authors declare that they have no known competing financial interests or personal relatonships that could have appeared to infuence the work reported in this paper.

CRediT authorship contribution statement

João Vargas: Conceptualization, Methodology, Software, Validation, Formal analysis, Investigation, Data curation, Visualization. **Bruno Lopez:** Software, Resources, Supervision. **Mário Lino da Silva:** Conceptualization, Methodology, Software, Validation, Formal analysis, Investigation, Resources, Data curation, Visualization, Supervision.

Acknowledgments

The authors acknowledge Dr. A. Lemal for correspondence taken place during this work. The authors would also extend their acknowledgment to Dr. E. Pannier and Dr. C. Laux for suggestions and further correspondence over the course of this work. The authors also acknowledge Dr. A. Brandis for inputs regarding past works on $\mathtt{CO}_2$ radiation. Finally the authors are warmly indebted Dr. B. Cruden who kindly supplied the CFD profile for the simulated shock-tube experiments. This work has been partially supported by the Portuguese FCT, under Projects UID/FIS/50010/2019 and the grant PD/BD/114325/2016 (PD-F APPLAuSE) and ESA project “Standard kinetic models for $\mathtt{CO}_2$ dissociating flows” (RFQ314355/15/NL/KML/FG).

References

[1] Lino Da Silva M, Beck J. Contribution of co_2 ir radiation to martian entries radiative wall fluxes. 49th AIAA Aerospace Sci Meet Includ New Horizons Forum Aerospace Exposit 2011. doi:10.2514/6.2011-135.

[2] Cruden B, Brandis A, R White T, Mahzari M, Bose D. Radiative heating during mars science laboratory entry: simulation, ground test, and flight. J Thermophys Heat Transfer 2016;30:1–9. doi:10.2514/1.T4798.

[3] Gordon IE, Rothman LS, Hill C, Kochanov RV, Tan Y, Bernath PF, Birk M, Boudon V, Campargue A, Chance KV, Drouin BJ, Flaud J-M, Gamache RR, Hodges JT, Jacquemart D, Perevalov VI, Perrin A, Shine KP, Smith M-AH, Tennyson J, Toon GC, Tran H, Tyuterev VG, Barbe A, Császár AG, Devi VM, Furtenbacher T, Harrison JJ, Hartmann J-M, Jolly A, Johnson TJ, Karman T, Kleiner I, Kyuberis AA, Loos J, Lyulin OM, Massie ST, Mikhailenko SN, Moazzen-Ahmadi N, Müller HSP, Naumenko OV, Nikitin AV, Polyansky OL, Rey M, Rotger M, Sharpe SW, Sung K, Starikova E, Tashkun SA, Vander Auwera J, Wagner G, Wilzewski J, Wcislo P, Yu S, Zak EJ. The hitran2016 molecular spectroscopic database. Journal of Quantitative Spectroscopy and Radiative Transfer 2017;203:3–69. doi:10.1016/j.jqsrt.2017.06.038. HITRAN2016 Special Issue.

[4] Rothman L, Gordon I, Barber R, Dothe H, Gamache R, Goldman A, et al. HITEMP, the high-temperature molecular spectroscopic database. Journal of Quantitative Spectroscopy and Radiative Transfer 2010;111(15):2139–50. doi:10.1016/j.jqsrt.2010.05.001. XVIth Symposium on High Resolution Molecular Spectroscopy (HighRus-2009).

[5] Lino da Silva M., Lopez B., Espinho S.. SPARTAN 3.0 User Manual; 2019.

[6] Tashkun S, Perevalov V. Cdsd-4000: high-resolution, high-temperature carbon dioxide spectroscopic databank. J Quant Spectrosc Radiat Transfer 2011;112(9):1403–10. doi:10.1016/j.jqsrt.2011.03.005.

[7] Vargas J, Lopez B, Panesi M, Lino da Silva M. Refitting of detailed CO_2 ir databases to vibrationally specific databases tailored for aerothermodynamic flows. In: 2018 Joint Thermophysics and Heat Transfer Conference. American Institute of Aeronautics and Astronautics Inc, AIAA; 2018. ISBN 9781624105524
[8] Bernath P. Spectra of Atoms and Molecules. Oxford University Press; 2016. ISBN 9780199382576.
[9] Counil J, Bonneville R, Rocard F. The french involvement in Mars sample return program. In: 34th COSPAR Scientific Assembly. In: COSPAR Meeting, 34; 2002. p. 3166.
[10] Harvey B. Europe's Space programme: to Arianne and Beyond. Springer Praxis Books. Springer London; 2003. ISBN 9781852337223.
[11] Messina P, Vennemann D. The European Space exploration programme: current status of ESA's plans for Moon and Mars exploration. Acta Astronaut 2005;57(2–8):156–60.
[12] Reynier P. Survey of aerodynamics and aerothermodynamics efforts carried out in the frame of Mars exploration projects. Prog Aerosp Sci 2014;70:1–27. doi:10.1016/j.paerosci.2014.03.004.
[13] Blanchard RC, Walberg GD. Determination of the hypersonic-continuum/rarefied-flow drag coefficient of the viking lander capsule 1 aeroshell from flight data. NASA Technical Paper 1793 1980.
[14] Ingoldby R, Michel F, Flaherty T, Doryand M, Preston B, Villyard K, et al. Entry data analysis for viking landers 1 and 2 final report. NASA CR-159388 1976.
[15] Beck J. ExoMars aerodynamics and aerothermodynamics: Viking flowfield calculations for radiative assessment. Tech. Rep.. ESA, EXM-DM-AE-FGE-RAD01; 2010.
[16] Lino da Silva M. ExoMars aerodynamics and aerothermodynamics assesment of the radiative heat fluxes on the viking spacecraft backcover. Tech. Rep.. ESA, EXM-DM-TNO-IST-0001; 2011.
[17] Gupta RN, Lee KP, Scott CD. Aerothermal study of Mars pathfinder aeroshell. J Spacecr Rockets 1996;33(1):61–9. doi:10.2514/3.55708.
[18] Hollis B, Perkins J. Hypervelocity aeroheating measurements in wake of Mars mission entry vehicle. In: Fluid Dynamics Conference; 1995.
[19] Hollis BR, Perkins JN. High-enthalpy aerothermodynamics of a Mars entry vehicle part 1: experimental results. J Spacecr Rockets 1997;34(4):449–56. doi:10.2514/2.3257.
[20] Edquist K, Dyakonov A, Wright M, Tang C. Aerothermodynamic environments definition for the Mars science laboratory entry capsule, 20; 2007. doi:10.2514/6.2007-1206. ISBN 978-1-62410-012-3.
[21] Hollis B, Borrelli S. Aerothermodynamics of blunt body entry vehicles: Assessment of aerothermodynamic flight prediction tools through ground and flight experimentation. Tech. Rep.. RTO - NATO Technical Report; 2011.
[22] O'Neil W, Cazaux C. Mars sample return project. Acta Astronaut 2000;47:453–65. doi:10.1016/S0094-5765(00)00085-0.
[23] Fraysse H, Powell R, Rousseau S, Striepe S. CNES-NASA studies of the mars sample return orbiter aerocapture phase. 51st International Astronautical Congress; 2000.
[24] Bonneville R, Rocard F, Counil J-L. French involvement in Mars exploration. Acta Astronautica 2002;51(1):329–35. doi: 10.1016/S0094-5765(02)00068-1.
[25] Chabut E. Simulation aérothermodynamique en régime d'écoulement raréfié par méthode de Monte-Carlo. Université d'Orléans; 2005. Thèse de doctorat Physique des gaz et des plasmas Orléans 2005.
[26] Lino da Silva M. Simulation des propriétés radiatives du plasma entourant un véhicule traversant une atmosphère planétaire à vitesse hypersonique: Application à la planète Mars. Université d'Orléans; 2004.
[27] Warmbein B, editor. Proceedings of the First International Workshop on Radiation of High Temperature Gases in Atmospheric Entry. ESA Publications Division; 2003. ISBN 92-9092-843-3.
[28] Fletcher K, editor. Proceedings of the First International Workshop on Radiation of High Temperature Gases in Atmospheric Entry - part II. ESA Publications Division; 2005. ISBN 92-9092-894-8
[29] Wilson A, editor. Proceedings of the 2nd International Workshop on Radiation of High Temperature Gases in Atmospheric Entry. ESA Publications Division; 2006. ISBN 92-9092-940-5.
[30] Lacoste H, Ouwehand L, editors. Proceedings of the 3rd International Workshop on Radiation of High Temperature Gases in Atmospheric Entry. ESA Publications Division; 2009. ISBN 978-92-9221-231-5.
[31] Lacoste-Francis H, editor. Proceedings of the 4th International Workshop on Radiation of High Temperature Gases in Atmospheric Entry. ESA Publications Division; 2011. ISBN 978-92-9092-253-7.
[32] Ouwehand L, editor. Proceedings of the 5th International Workshop on Radiation of High Temperature Gases in Atmospheric Entry. ESA Publications Division; 2012. ISBN 978-92-9092-278-0.
[33] 6th international workshop on radiation of high temperature gases in atmospheric entry. St. Andrews, 2014, http://www-solar.mcs.st-and.ac.uk/~rhtg6/.
[34] 7th international workshop on radiation of high temperature gases in atmospheric entry. Stuttgart, 2016, http://www.irs.unistuttgart.de/rhtg/downloads/IRS_RadiationWS7_2nd_announcement_MA.pdf retrieved: 1/1/2018.
[35] 8th international workshop on radiation of high temperature gases in atmospheric entry. Madrid, 2019, url: https://indico.esa.int/event/272/
[36] Charbonnier J, Couzi J, Dieudonné W, Vérant J. Definition of an axially symmetric testcase for high temperature gas radiation prediction in Mars atmosphere entry. Rapport CNES NG104-07-TF-001-CNES 2003.
[37] Charbonnier J-M. Analysis of the results for TC3 presented at the 1st international workshop on radiation of high temperature gas in planetary atmosphere entry. In: Radiation of high temperature gases in atmospheric entry, 533; 2003. p. 145–59.
[38] Rouzaud O, Zlukhtov S, Egorov I, Fletcher D, Gromov V, Nagnibeda E, et al. Numerical, analytical and experimental investigation of convective and radiative heating of a martian descent module. In: Fletcher K, editor. Radiation of high temperature gases in atmospheric entry. ESA Special Publication, 583; 2005. p. 93.
[39] Egorov I., Borovoy V., Skuratov A.. Afterbody convective heating of a Martian descent vehicle. In: 48th AIAA Aerospace sciences meeting including the new horizons forum and aerospace exposition, doi:10.2514/6.2010-1073.
[40] Soufiani A, Taine J. High temperature gas radiative property parameters of statistical narrow-band model for H_2O, CO_2 and CO, and correlated-k model for H_2O and CO_2. Int J Heat Mass Transf 1997;40(4):987–91. doi:10.1016/0017-9310(96)00129-9.
[41] Aguir M, Perrin M, Taine J. Variational calculation of energies of highly excited rovibrational states of 12c16o2. J Mol Spectrosc 2002;215(2):234–43. doi:10.1006/jmsp.2002.8641.
[42] Scutaru D, Rosenmann L, Taine J. Approximate intensities of CO_2 hot bands at 2.7, 4.3, and 12μm for high temperature and medium resolution applications. J Quant Spectrosc Radiat Transfer 1994;52(6):765–81. doi:10.1016/0022-4073(94)90042-6.
[43] Perrin M, Rivière P, Soufiani A. Radiation database for Earth and Mars entry. Tech. Rep. RTO - NATO Technical Report; 2008. doi:10.14339/RTO-EN-AVT-162.
[44] Rivière P, Soufiani A, Perrin MY. Line by line and statistical narrow-band calculations of radiative transfer in some atmospheric entry problems. ESA (Special Publication) 2003;533:189–96.
[45] Gromov V, Surzhikov S. Convective and radiative heating of a martian space vehicle base surface. In: Harris RA, editor. Proceedings of the Fourth symposium on aerothermodynamics for space vehicles. ESA Special Publication, 487; 2002. p. 265.
[46] Surzhikov S.. Numerical Simulation of heat radiation generated by entering space vehicle, doi:10.2514/6.2004-2379.
[47] Surzhikov ST. Radiative-gasdynamic model of a Martian descent Space vehicle. 42nd AIAA Aerospace sciences meeting and exhibit; 2004.
[48] Surzhikov S. TC3: Convective and radiative heating of MSRO for simplest kinetic models. In: Fletcher K, editor. Proceedings of the first international workshop on radiation of high temperature gases in atmospheric Entry - Part II. ESA Special Publication, 583; 2005. p. 55.
[49] Andrienko D, Surzhikov S. Radiative heating of Martian space vehicle at crucial points of trajectory. In: 49th AIAA Aerospace sciences meeting including the new horizons forum and aerospace exposition; 2011. p. 246.
[50] Surzhikov S. Comparative analysis of radiative aerothermodynamics of martian entry probes. In: 43rd AIAA thermophysics conference; 2012. p. 2867.
[51] Flamment C. Ecoulements de fluide visqueux de desequilibre chimique et vibrationnel modelisation, applications internes et externes. Université Pierre et Marie Curie; 1990. Thèse Doctorat Physique Paris 6 1990
[52] William J. Etude des processus physico-chimiques dans les écoulements détendus à haute enthalpie application à la soufflerie à arc f4. Université de Provence; 1999. Thèse de doctorat Physique Aix-Marseille 1 1999
[53] Tessé L. Modélisation des transferts radiatifs dans les flammes turbulentes par une méthode de monte carlo. Ecole centrale de Paris; 2001. Thèse de doctorat Energétique Châtenay-Malabry
[54] Tessé L, Dupoirieux F, Zamuner B, Taine J. Radiative transfer in real gases using reciprocal and forward monte carlo methods and a correlated-k approach. Int J Heat Mass Transf 2002;45(13):2797–814. doi:10.1016/S0017-9310(02)00009-1.
[55] Tessé L, Dupoirieux F, Taine J. Monte Carlo modeling of radiative transfer in a turbulent sooty flame. Int J Heat Mass Transf 2004;47(3):555–72. doi:10.1016/j.ijheatmasstransfer.2003.06.003.
[56] Rouzaud O, Tesse L, Soubrie T, Soufiani A, Riviere P, Zeitoun D. Influence of radiative heating on a Martian orbiter. J Thermophys Heat Transfer 2008;22(1):10–19. doi:10.2514/1.28259.
[57] Lino da Silva M. An adaptive line-by-line statistical model for fast and accurate spectral simulations in low-pressure plasmas. J Quant Spectrosc Radiat Transfer 2007;108(1):106–25. doi:10.1016/j.jqsrt.2007.03.005.
[58] Rothman L, Gamache R, Tipping R, Rinsland C, Smith M, Benner D, et al. The hitran molecular database: Editions of 1991 and 1992. Journal of Quantitative Spectroscopy and Radiative Transfer 1992;48(5):469–507. doi:10.1016/0022-4073(92)90115-K. Special Issue Conference on Molecular Spectroscopic Databases
[59] Lino da Silva M. A contribution for the simulation of VUV-IR radiation transfer in CO_2-N_2 entry flows using a line-by-line model. In: Proceedings of the 4th international workshop on radiation of high temperature gases in atmospheric entry, 689; 2011.
[60] Lino da Silva M., Sobia R., Witasse O. Radiative trail of the phoenix entry. In: 47th AIAA Aerospace sciences meeting including the new horizons forum and aerospace exposition. doi:10.2514/6.2009-1032.
[61] Witasse O, Lino da Silva M, Sobbia R, Leyland P, Marraffa L, Schmitz P, et al. Mars express observation of the phoenix entry: simulations, planning, results and lessons learned. CEAS Space J 2014;6. doi:10.1007/s12567-013-0051-8.
[62] Beck J, Omaly P, Lino da Silva M, Surzhikov S. Radiative heating of the ExoMars entry demonstrator module. Proceedings of the 7th European Symposium on Aerothermodynamics 2011:9.
[63] Lino da Silva M, Beck J. Contribution of CO_2 IR radiation to Martian entries radiative wall fluxes. In: 49th AIAA Aerospace sciences meeting including the new horizons forum and aerospace exposition. ISBN 978-1-60086-950-1; doi:10.2514/6.2011-135.
[64] Gülhan A, Thiele T, Siebe F, Kronen R, Schleutker T. Aerothermal measurements

from the ExoMars Schiaparelli capsule entry. J Spacecr Rockets 2019;56(1):68–81. doi:10.2514/1.A34228.

[65] Bogdanoff D. Shock tube experiments for earth and mars entry conditions. Non-Equilibrium Gas Dynamics - From Physical Models to Hypersonic Flights, The Research and Technology Organisation (RTO) of NATO Educational Notes, 2009 2009. doi:10.14339/RTO-EN-AVT-162.

[66] Cruden B, Prabhu D, Martinez R. Absolute radiation measurement in high mass venus and Mars entry conditions. J Spacecr Rockets 2012;49:1069–79. doi:10.2514/1.60916.

[67] SUndberg L, Duff J, Bernstein L. Nonequilibrium infrared emission model for the wake flow of re-entry vehicles. J Spacecr Rockets 1993;30(6):731–41. doi:10.2514/3.26379.

[68] Palmer G, Cruden B. Experimental validation of CO_2 radiation simulations; 2012. doi:10.2514/6.2012-3188. ISBN 978-1-62410-186-1.

[69] Cruden B, Brandis A, Prabhu D. Measurement and characterization of mid-wave infrared radiation in CO_2 shocks; 2014. doi:10.2514/6.2014-2962. ISBN 978-1-62410-281-3.

[70] Brandis AM, Cruden BA, White TR, Saunders DA, Johnston CO. Radiative heating on the after-body of martian entry vehicles. In: 45th AIAA Thermophysics Conference, doi:10.2514/6.2015-3111.

[71] Cruden B, Brandis A, White T, Bose D. Radiative Heating for MSL Entry: verification of Simulations from Ground Test to Flight Data, doi:10.2514/6.2015-1894.

[72] Brandis A, White TR, Saunders D, Hill J, Johnston CO. Simulation of the schiaparelli entry and comparison to aerothermal flight data. AIAA Aviation 2019 Forum; 2019. doi:10.2514/6.2019-3260.

[73] Tashkun S, Perevalov V, Teffo J-L, Bykov A, Lavrentieva N. CDSD-1000, the high-temperature carbon dioxide spectroscopic databank. Journal of Quantitative Spectroscopy and Radiative Transfer 2003;82(1):165–96. doi:10.1016/S0022-4073(03)00152-3. The HITRAN Molecular Spectroscopic Database: Edition of 2000 Including Updates of 2001

[74] Potter D. Photaura User Guide; 2013.

[75] M Osipov V. Partition sums and dissociation energy for 12C16O2 at high temperatures. Mol Phys 2004;102:1785–92 http://cfcfd.mechmining.uq.edu.au/photaura.html.

[76] Mikhailenko G, Babikov S, Yu L. Information-calculating system spectroscopy of atmospheric gases. the structure and main functions.. Atmos Oceanic Opt 2005;18(9):685–95.

[77] Lemal A, Takayanagi H, Nomura S, Fujita K. Simulations of carbon-dioxide equilibrium infrared radiation measurements. J Thermophys Heat Transfer 2018;32(1):184–95. doi:10.2514/1.T5134.

[78] Pannier E, Laux C. Analysis of the JAXA nonequilibrium infrared emission spectra for mars entry conditions. J Thermophys Heat Transfer 2019:1–5. doi:10.2514/1.T5646.

[79] Takayanagi H, Lemal A, Nomura S, Fujita K. Measurements of carbon dioxide nonequilibrium infrared radiation in shocked and expanded flows. J Thermophys Heat Transfer 2018;32:483–94. doi:10.2514/1.T5200.

[80] Pannier E, Laux C. RADIS: a nonequilibrium line-by-line radiative code for CO_2 and HITRAN-like database species. J Quant Spectrosc Radiat Transfer 2018;222. doi:10.1016/j.jqsrt.2018.09.027.

[81] Lee E-S, Park C, Chang K-S. Shock-tube determination of CN formation rate in a CO-N2 mixture. J Thermophys Heat Transfer 2007;21(1):50–6. doi:10.2514/1.25144.

[82] Cruden B, Brandis A, MacDonald M. Characterization of CO thermochemistry in incident shockwaves. In: 2018 Joint Thermophysics and Heat Transfer Conference, doi:10.2514/6.2018-3768.

[83] Cruden B. Test-case for mid-infrared radiation prediction in MSL-similar shock tube test. 2019.

[84] Depraz S, Perrin M, Soufiani A. Infrared emission spectroscopy of CO_2 at high temperature. part i: experimental setup and source characterization. J Quant Spectrosc Radiat Transfer 2012;113:1–13.

[85] Depraz S, Perrin MY, Rivière P, Soufiani A. Infrared emission spectroscopy of CO_2 at high temperature. Part II: experimental results and comparisons with spectroscopic databases. J Quant Spectrosc Radiat Transfer 2012;113:14–25.

[86] SPARK Line-by-line code, http://esther.ist.utl.pt/sparklbl/. Accessed: 20th January 2020.